

GRB 140102A: Insight into Prompt Spectral Evolution and Early Optical Afterglow Emission

Rahul Gupta,^{1,2*} S. R. Oates,³ S. B. Pandey,^{1†} A. J. Castro-Tirado,^{4,5} Jagdish C. Joshi,^{6,7} Y.-D. Hu,^{4,8} A. F. Valeev,^{9,10} B. B. Zhang,^{6,7} Z. Zhang,⁶ Amit Kumar,^{1,11} A. Aryan,^{1,2} A. Lien,^{12,13} B. Kumar,¹ Ch. Cui,¹⁴ Ch. Wang,¹⁵ Dimple,^{1,2} D. Bhattacharya,¹⁶ E. Sonbas,¹⁷ J. Bai,¹⁵ J. C. Tello,⁴ J. Gorosabel,^{†4,18,19} J. M. Castro Cerón,²⁰ J. R. F. Porto,²¹ K. Misra,¹ M. De Pasquale,^{22,23} M. D. Caballero-García,⁴ M. Jelínek,^{4,24} P. Kubánek,²⁵ P. Yu. Minaev,²⁶ R. Cunniffe,⁴ R. Sánchez-Ramírez,²⁷ S. Guziy,^{28,29} S. Jeong,⁴ S. N. Tiwari,² S. Razzaque,³⁰ V. Bhalerao,³¹ V. C. Pintado,³² V. V. Sokolov,⁹ X. Zhao,¹⁵ Y. Fan,¹⁵ and Y. Xin¹⁵

Accepted 2021 May 26. Received 2021 May 22; in original form 2021 February 19

ABSTRACT

We present and perform a detailed analysis of multi-wavelength observations of GRB 140102A, an optical bright GRB with an observed reverse shock (RS) signature. Observations of this GRB were acquired with the BOOTES-4 robotic telescope, the *Fermi*, and the *Swift* missions. Time-resolved spectroscopy of the prompt emission shows that changes to the peak energy (E_p) tracks intensity and the low-energy spectral index seems to follow the intensity for the first episode, whereas this tracking behavior is less clear during the second episode. The fit to the afterglow light curves shows that the early optical afterglow can be described with RS emission and is consistent with the thin shell scenario of the constant ambient medium. The late time afterglow decay is also consistent with the prediction of the external forward shock (FS) model. We determine the properties of the shocks, Lorentz factor, magnetization parameters, and ambient density of GRB 140102A, and compare these parameters with another 12 GRBs, consistent with having RS produced by thin shells in an ISM-like medium. The value of the magnetization parameter ($R_B \approx 18$) indicates a moderately magnetized baryonic dominant jet composition for GRB 140102A. We also report the host galaxy photometric observations of GRB 140102A obtained with 10.4m GTC, 3.5m CAHA, and 3.6m DOT telescopes and find the host (photo $z = 2.8^{+0.7}_{-0.9}$) to be a high mass, star-forming galaxy with a star formation rate of $20 \pm 10 M_\odot \text{ yr}^{-1}$.

Key words: gamma-ray burst: general, gamma-ray burst: individual: GRB 140102A, methods: observational, shock waves.

1 INTRODUCTION

Gamma-ray Burst (GRB) emission can be divided into two phases: a short-lived and highly variable, initial prompt γ -ray emission phase, and a long-lived multi-wavelength afterglow emission phase (Piran 2004; Gehrels & Razzaque 2013; Kumar & Zhang 2015). Based on the observed duration of the prompt emission, GRBs are classified into two broad classes (Kouveliotou et al. 1993): long GRBs (LGRBs: $T_{90}^1 > 2$ sec) and short GRBs (SGRBs: $T_{90} \leq 2$

sec). It implies a distinction between their progenitors (Levan et al. 2016). The LGRBs are associated with the deaths of massive stars (MacFadyen & Woosley 1999; Woosley & Bloom 2006; Davies et al. 2007; Obergaulinger & Aloy 2020) and SGRBs with the mergers of compact binary objects such as two neutron stars or a neutron star and black hole (Perna & Belczynski 2002; Belczynski et al. 2002; Abbott et al. 2017; Goldstein et al. 2017). There is, however, a significant overlap between the bi-modal duration distribution of GRBs (Kouveliotou et al. 1993; Qin & Chen 2013; Goldstein et al. 2017; Li et al. 2016; Minaev & Pozanenko 2017). A doubtful third class with intermediate duration is also proposed (Mukherjee et al. 1998; Hakkila et al. 2000; Chattopadhyay et al. 2007; Horváth et al. 2008; Minaev et al. 2010; Horváth & Tóth 2016).

* E-mail: rahulbhu.c157@gmail.com, rahul@aries.res.in

† shashi@aries.res.in

¹ T_{90} is the duration during which 5 percent to 95 percent of the γ -ray/hard X-ray fluence is received.

The prompt emission in GRBs is believed to be produced in a relativistic jet via energy dissipation in internal shocks when fast-moving shells catch-up with slower shells or due to catastrophic reconfiguration of the magnetic fields in a Poynting flux dominated outflow (Pe’er 2015; Lyutikov & Blackman 2001). The radiation physics of the prompt emission is still under debate (Kumar & Zhang 2015). The prompt emission may be explained as synchrotron emission from a cooling population of particles (Oganesyan et al. 2019; Burgess et al. 2020; Zhang 2020). However, photospheric models also can equally well explain the data (Vianello et al. 2017; Ahlgren et al. 2019; Acuner et al. 2020).

Examining the prompt emission spectral evolution is a powerful tool to investigate the radiation mechanisms of GRBs (Pe’er 2015). The evolution of peak energy has been observed to have three types of patterns: (i) a hard-to-soft pattern, where E_p decreases continuously (Norris et al. 1986; Bhat et al. 1994; Band 1997); (ii) an intensity-tracking pattern, where E_p increases/decreases as the intensity increases/decreases (Golenetskii et al. 1983; Ryde & Svensson 1999); (iii) a soft-to-hard pattern or disordered pattern, where E_p increases continuously or does not show any correlation with flux (Laros et al. 1985; Kargatis et al. 1994). Uhm et al. (2018) reproduced the hard-to-soft and intensity-tracking patterns using a synchrotron radiation model in a bulk-accelerating emission region. Furthermore, they suggested a direct connection between these two patterns (hard-to-soft and intensity-tracking) and spectral lags. They predicted that only the positive spectral lag could be observed for the hard-to-soft pattern, but both positive and negative spectral lags are possible in the case of intensity-tracking. Minaev et al. (2014) suggested that individual pulses of GRBs demonstrate hard-to-soft spectral evolution (positive spectral lags), depending on the pulse duration. A complicated spectral evolution behavior could be connected with superposition effects. The low energy spectral index (α_{pt}) evolves with time but does not exhibit any strong typical pattern (Crider et al. 1997). Recently, Li et al. (2019) found that both E_p and α_{pt} show an intensity-tracking pattern (‘double-tracking’) for GRB 131231A.

The relativistically moving blastwave inevitably crashes into the circumburst medium and results in external shocks. The afterglow phase, in general, is well explained by the emission originating in these external shocks, and any deviations from this model can generally be explained (e.g., see Kumar & Zhang 2015; Mészáros 2019 for a review). According to the standard afterglow model, the external shocks can be divided into two forms: a long-lived forward shock that propagates into the circumburst medium and produces a broadband afterglow, and a short-lived RS that propagates into the ejecta and produces a short-lived optical flash and a radio flare (Zhang et al. 2003b; Nakar & Piran 2004; Gao & Mészáros 2015). For most GRBs, the FS component can generally explain the observed afterglow. Investigations of the afterglow using the FS model offer detailed information about the late time afterglow emission, jet geometry, circumburst medium, and total energy (Panaitescu 2007; Wang et al. 2015; Joshi & Razzaque 2019). On the other hand, the short-lived RS emission is useful in probing the nature of magnetization and composition of GRB ejecta from the central engine (Gao & Mészáros 2015). RS emission has mainly two types of evolution (Kobayashi & Sari 2000): In the first situation, RS is relativistic enough to decelerate the shell (thick shell case, $T_{90} > T_{dec}$ where T_{dec} is the deceleration time defined as $T_{dec} = (3E_k(1+z)^3/32\pi n_0 m_p \Gamma_0^8 c^5)^{1/3}$, for blast-wave kinetic energy (E_k), initial Lorentz factor (Γ_0), traversing into a constant density circumburst medium with density (n_0) (Zhang et al. 2003a). The blast-wave radius evolves with time and it is defined as $R_{dec}(t = T_{dec}) \approx 2cT_{dec}\Gamma_0^2/(1+z)$.

On the other hand, for the thin shell case ($T_{90} < T_{dec}$), the RS could be sub-relativistic and too weak to decelerate the shell (Gao et al. 2015). It has been found that most of the GRBs with early optical RS signatures could be explained well within the thin shell case (Japelj et al. 2014; Gao et al. 2015; Yi et al. 2020).

Fast optical follow-up of GRBs is vital for detecting and studying the relatively early and short-lived RS component. GRB 990123, the first burst with a simultaneous optical flash as the signature of RS was detected using the Robotic Optical Transient Search Experiment (ROTSE)-I telescope (Akerlof et al. 1999; Mészáros & Rees 1999). The RS emission has been observed for only a few GRBs, even after rapid follow-up observations by the *Swift* Ultra-Violet and Optical Telescope (UVOT; Roming et al. 2005) and other ground-based robotic telescopes network (Zhang et al. 2003b; Oates et al. 2009). The lack of observed RS could be due to strongly magnetized outflows such that the RS component of the external shock is suppressed, either the RS emission component peaks at frequencies lower than optical frequencies and is thus generally missed, and/or the RS emission originating in external shock is masked by the prompt emission originating in an internal shock (Zhang & Kobayashi 2005; Resmi & Zhang 2016; Kopač et al. 2013).

In a comprehensive sample (118 GRBs with known redshift) by Japelj et al. (2014), 10 bursts² showed dominant RS signatures originated from external shock with most of these having an ISM-like external medium (constant density). At late times (> 10 ks), the RS emission showed magnetization parameters³ ($R_B \sim 2$ to 10^4) and was fainter than average optical FS emission (Japelj et al. 2014). Gao et al. (2015) identified 15 GRBs with RS signatures based on a morphological analysis of the early optical afterglow light curves of 63 GRBs and an estimated $R_B \sim 100$. More recently, Yi et al. (2020) studied the early optical afterglows of 11 GRBs⁴ with RS emission signatures. They found that the external medium density w.r.t. blast-wave radius follows a power-law type behavior with index (k) ranges in between 0 to 1.5. Among other shock parameters, the densities of the external medium for thin shell RS dominated bursts are compared in this work (see § 4.2) and shown to vary in a range 0.1 – 500 cm^{-3} .

In this paper, we present multiwavelength data and analysis of GRB 140102A including our early optical afterglow observations using Burst Observer and Optical Transient Exploring System (BOOTES)-4 robotic telescope starting ~ 29 sec after the *Fermi* Gamma-Ray Burst Monitor (GBM; also the *Swift* Burst alert telescope (BAT) at the same time) trigger (T_0). The very early detection of optical emission from GRB 140102A along with GeV Large Area Telescope (LAT) detection inspired us to study this burst in detail and compare it with other similar events. This paper is organized as follows. In § 2, we discuss the multiwavelength observations and data analysis. The main results are presented in § 3. This is followed by discussion in § 4 and finally summary and conclusion in § 5, respectively. All the uncertainties are quoted at 1σ throughout this paper unless otherwise mentioned. The temporal (α) and spectral indices (β) for the afterglow are given by the expression $F(t, \nu) \propto t^{-\alpha} \nu^{-\beta}$. We consider the Hubble parameter $H_0 = 70$ $\text{km sec}^{-1} \text{Mpc}^{-1}$, density parameters $\Omega_\Lambda = 0.73$, and $\Omega_m = 0.27$.

² GRBs 990123, 021004, 021211, 060908, 061126, 080319B, 081007, 090102, 090424, and 130427A

³ It is the ratio between $\epsilon_{B,r}$ (fraction of reverse shock energy into the magnetic field) and $\epsilon_{B,f}$ (fraction of forward shock energy into the magnetic field), respectively.

⁴ GRBs 990123, 041219A, 060607A, 061007, 081007, 081008, 090102, 110205A, 130427A, 140512A, and 161023A

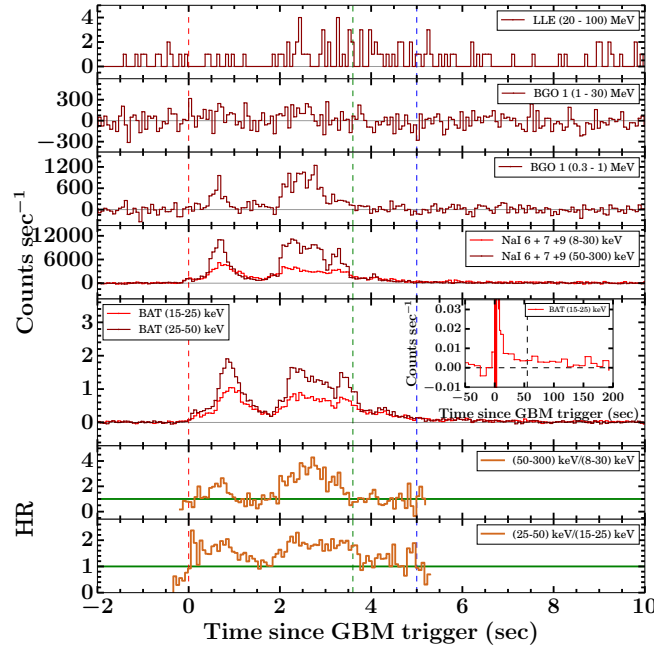


Figure 1. Multi-channel prompt γ -ray/hard X-ray light curve: The top five panels show the background-subtracted light curve of GRB 140102A in multiple energy channels of *Fermi* LLE, *Fermi* GBM, and *Swift* BAT detectors with 64 ms temporal bins. The red and green vertical dashed lines indicate the *Fermi* trigger time and end of T_{90} duration for *Fermi* GBM detector in 50-300 keV energy range, respectively. The blue vertical dashed line indicates the end time of the time-averaged spectral analysis, with the start time taken as T_0 . The horizontal grey solid lines differentiate between signal and background (at count rate equal to zero). Inset shows the BAT light curve in the soft (15-25 keV) energy band with 3' or 10 sec temporal binning. It indicates the presence of soft tail emission in the *Swift* BAT light curve. The vertical black dashed line represents the T_{90} end time for *Swift* BAT detector in 15-350 keV energy range. **Evolution of hardness ratio (HR) :** The last two panels show the evolution of HR in 50-300 keV (hard) to 8-30 keV (soft) energy channels of *Fermi* sodium iodide (NaI 6 + 7 + 9) and in 25-50 keV (hard) to 15-25 keV (soft) energy channels of *Swift* BAT detectors, respectively. The horizontal green solid line corresponds to HR equal to one.

2 MULTI-WAVELENGTH OBSERVATIONS & DATA ANALYSIS

2.1 Gamma-ray/ Hard X-ray observations

GRB 140102A triggered the BAT (Barthelmy et al. 2005) on board the *Neil Gehrels Swift* observatory (Gehrels et al. 2004) on January 02, 2014 at 21:17:37 UT. The best on-ground location was found to be RA, Dec = 211.902, +1.331 degrees (J2000) with 3' uncertainty with 90% containment (Hagen et al. 2014). The GBM (Meegan et al. 2009) on board *Fermi* Gamma-Ray Space Telescope triggered at 21:17:37.81 UT (T_0). The *Fermi* GBM light curve shows two bright overlapping peaks (see Figure 1) with a T_{90} duration of 3.6 ± 0.1 sec in the 50 - 300 keV energy range (Narayana Bhat et al. 2016). For a time interval from $T_0 + 0.4$ to $T_0 + 4$ sec, the time-averaged spectrum is best described with the Band model (Band et al. 1993) with $\alpha_{pt} = -0.71 \pm 0.02$, high energy spectral index $\beta_{pt} = -2.49 \pm 0.07$, and $E_p = 186 \pm 5$ keV. In this time interval, an energy fluence of $1.78 \pm 0.03 \times 10^{-5}$ erg cm $^{-2}$ is calculated in the 10-10000 keV energy band (Zhang & Bhat 2014). This fluence value is among the top 12 percent most bright GRBs observed by the *Fermi*-GBM, making this burst suitable for detailed analysis. The LAT (Atwood et al. 2009) on board *Fermi* triggered at 21:17:37.64 UT and detected high energy emission from GRB 140102A. The best *Fermi*-LAT on-ground location (RA, DEC = 211.88, 1.36 (J2000)) was at 47° from the LAT boresight angle at T_0 and the highest-energy photon with a energy of 8 GeV is detected 520 sec after T_0 (Sonbas et al. 2014).

Other gamma-ray/hard X-ray space telescopes such as

Table 1. Prompt emission properties of GRB 140102A. Redshift has been obtained using the SED modeling at 700 - 1000 sec (see § 2.5). The peak flux is calculated in the 1-10,000 keV energy range in the source frame.

Prompt Properties	GRB 140102A	Detector
T_{90} (sec)	3.58 ± 0.01	GBM
t_{mvt} (sec)	~ 0.20	GBM
HR	1.05 ± 0.02	GBM
E_p (keV)	$186.57^{+4.16}_{-4.51}$	BAT+GBM+LLE+LAT
F_p	$8.90^{+11.0}_{-5.0}$	GBM
$E_{\gamma,iso}$ (erg)	$7.14^{+0.36}_{-0.31} \times 10^{53}$	-
$L_{\gamma,iso}$ (erg sec $^{-1}$)	$2.78^{+3.44}_{-1.56} \times 10^{53}$	-
Redshift z	$2.02^{+0.05}_{-0.05}$	XRT + UVOT + BOOTES

T_{90} : Duration from GBM data in 50-300 keV; t_{mvt} : minimum variability time scale in 8-900 keV; HR: ratio of the counts in 50-300 keV to the counts in 10-50 keV; E_p : Time-integrated peak energy calculated using joint *Swift* BAT, *Fermi* GBM and LAT data; F_p : peak flux in 10^{-6} erg cm $^{-2}$; $E_{\gamma,iso}$: Isotropic γ -ray energy in the source frame; $L_{\gamma,iso}$: Isotropic γ -ray peak luminosity in the source frame. All the results presented in this table are obtained using different analyses methods discussed in § 2 and § 3.

MAXI/GSC (at 21:19:54 UT, Kimura et al. 2014) and *Konus-Wind* (at 21:17:36.245 UT; $T_{kw,0}$; Golenetskii et al. 2014) also detected GRB 140102A. For a time interval from $T_{kw,0}$ to $T_{kw,0} + 10.496$ sec, the time-averaged KW spectrum is best fitted with Band function (Band et al. 1993) with parameters $\alpha_{pt} = -1.05 \pm 0.14$, $\beta_{pt} = -2.68 \pm 0.30$, and $E_p = 185 \pm 19$ keV (Golenetskii et al. 2014).

2.1.1 *Fermi*-LAT analysis

We obtained the *Fermi*-LAT (Atwood et al. 2009) data within a temporal window extending up to 10000 sec after T_0 from *Fermi*-LAT data server⁵ using *gtburst*⁶ version 02-03-00p33 software. We performed unbinned likelihood analysis and selected a region of interest (ROI) of 12° around the enhanced *Swift* XRT position (Goad et al. 2014). Further, we filtered the high energy LAT emission by cutting on photons with energies in the range of 100 MeV-300 GeV. We also applied an angular cut of 100° between the source and zenith of the satellite in order to reduce the contamination of photons coming from the Earth limb. For the time-integrated duration, we used the P8R3_SOURCE_V2 response, which is appropriate for long durations ($\sim 10^3$ sec), and for the time-resolved bins, we used P8R2_TRANSIENT020E_V6 response, which is appropriate for small durations (Bruel et al. 2018). We included a point source (for GRB) at the location of the burst, considering a power-law spectrum, an isotropic component (to show the extragalactic background emission) *iso_P8R3_SOURCE_V2* and a Galactic diffuse component (to represent the Galactic diffuse emission) *gll_iem_v07*⁷. The probability of association of the photons with GRB 140102A is calculated using the *gtsrcprob* tool. For the total duration of 0-10000 sec, the energy and photon flux in 100-10000 MeV energy range are $(5.96 \pm 2.37) \times 10^{-10}$ erg cm⁻² sec⁻¹ and $(5.01 \pm 2.35) \times 10^{-7}$ ph. cm⁻² sec⁻¹, respectively, with a test-statistic (TS)⁸ of detection 46. The temporal distribution of *Fermi*-LAT photons with energies > 100 MeV along with the photon flux and the energy flux light curves is shown in Figure 2 (a). During the GBM time window, we obtained the LAT fluence value equal to $(0.18 \pm 0.10) \times 10^{-5}$ erg cm⁻² in 0.1-100 GeV energy range. We compared this value with the GBM fluence value for GRB 140102A along with other LAT detected GRBs (the second GRB LAT catalogue (2FLGC); Ajello et al. 2019; Akerlof et al. 2011). GRB 140102A lies on the line for which GBM fluence is 10 times brighter than LAT fluence for all the LAT detected sample (see Figure 2 (b)). Further, we also perform (see § 4.1.2) the time-resolved spectral analysis to investigate the origin of the high energy LAT photons (see Table A1 in appendix A).

2.1.2 *Fermi*-GBM analysis

The *Fermi*-GBM (Meegan et al. 2009) time-tagged event (TTE) data is downloaded from the GBM trigger data archive⁹. We investigated the temporal and spectral prompt emission properties of GRB 140102A using the three brightest sodium iodide (NaI 6, 7, and 9) and one brightest bismuth germanate (BGO 1) detectors. These detectors have source observing angles : NaI 9 - 31° , NaI 7 - 33° , NaI 6 - 35° , and BGO 1 - 42° . We obtained the multi-channel (energy-resolved) prompt emission light curve using RMFIT version

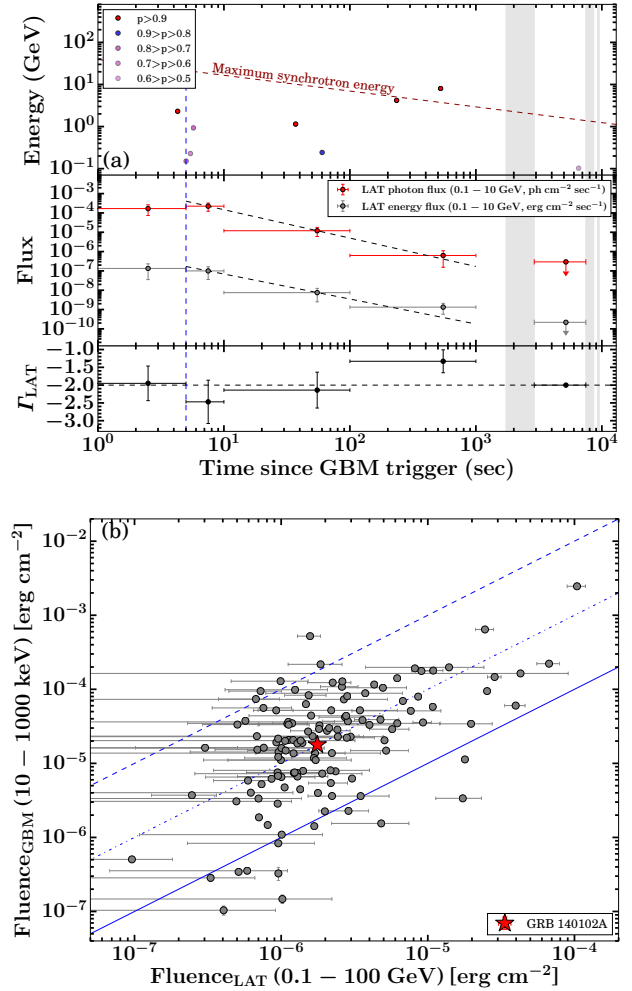


Figure 2. (a) Extended *Fermi*-LAT emission: *Top panel:* Temporal distribution of high energy LAT photons with energies > 100 MeV. The different colors of the photons represent their associated probabilities of originating from GRB 140102A. *Middle panel:* Evolution of *Fermi*-LAT energy (grey) and photon (red) fluxes in 100-10000 MeV range. In the last time bin, the LAT photon index was fixed to -2 to get an upper limit on the fluxes. The black dashed lines provide a power-law fit to the temporally extended photon flux and the energy flux light curves (for the photons detected 5 sec after T_0). *Bottom panel (b):* Temporal evolution of *Fermi*-LAT photon index in the 0.1-300 GeV range. The vertical blue dashed line corresponds similarly to Figure 1. The grey shaded region represents the source off-axis angle $> 65^\circ$. (b) Comparison of GBM and LAT fluence values for GRB 140102A along with LAT detected GRBs (Ajello et al. 2019). The solid line represents equal fluence, and dashed-dotted, dashed lines denote the fluence shifted by factors of 10 and 100, respectively.

⁵ <https://fermi.gsfc.nasa.gov/cgi-bin/ssc/LAT/LATDataQuery.cgi>

⁶ <https://fermi.gsfc.nasa.gov/ssc/data/analysis/scitools/gtbust.html>

⁷ <https://fermi.gsfc.nasa.gov/ssc/data/access/lat/BackgroundModels.html>

⁸ It is define as $TS = -2\ln L_{\text{max},0}/L_{\text{max},1}$, where $L_{\text{max},0}$ and $L_{\text{max},1}$ are the maximum likelihood value for a model without and with an additional source, respectively.

⁹ <https://heasarc.gsfc.nasa.gov/FTP/fermi/data/gbm/triggers/>

4.3.2 software¹⁰. The background-subtracted multi-channel prompt emission γ -ray/ hard X-ray light curves along with the hardness ratio are shown in Figure 1. The light curve consists of two major bright overlapping peaks. The HR shows that the first episode is softer than the subsequent episodes, which is also visible from the

¹⁰ <https://fermi.gsfc.nasa.gov/ssc/data/analysis/rmfir/>

very low signal for the first episode in LLE data¹¹ (Pelassa et al. 2010; Ajello et al. 2014, see appendix).

We created time-averaged spectra, using the `gtburst` software from the *Fermi* Science Tools, using the TTE mode data from the same detectors used for the temporal analysis. The main GRB emission duration (T_0 to $T_0 + 5$ sec) is selected for the time-averaged spectral analysis. The background is fitted by selecting two intervals, one prior to the burst and another after the burst. The spectral analyses are performed using X-Ray Spectral Fitting Package (XSPEC; Arnaud 1996) version 12.10.1 of `heasoft-6.25`. The statistics `pgstat` is used for optimization and testing the various models as *Fermi*-GBM data is Poisson in nature with Gaussian background. We modelled the data with traditional Band function. For the time-averaged spectrum obtained using GBM data only, we calculated $\alpha_{\text{pt}} = -0.75^{+0.04}_{-0.04}$, $\beta_{\text{pt}} = -2.57^{+0.14}_{-0.18}$, and $E_p = 185.42^{+9.54}_{-9.67}$ keV and these parameters are consistent with those determined by Zhang & Bhat (2014).

2.1.3 *Swift*-BAT analysis

We retrieved the *Swift*-BAT (Barthelmy et al. 2005) data from the Swift Archive Download Portal hosted by the UK Swift Science Data Centre¹². For the BAT data analysis, we used `HEASOFT` software version-6.25 with latest calibration database¹³. We began the reduction of BAT data from the raw files (Observation Id: 00582760000). We produced detector plane image (DPI) using `batbinevt` and identify the hot pixels with `bathotpix`. We applied mask-weighting (background subtraction) in the event file using the `batmaskwtevt` pipeline. The light curves is extracted using `batbinevt` tool. The energy resolved *Swift* BAT mask-weighted light curve is presented in Figure 1 along with the evolution of HR in 25-50 keV to 15-25 keV energy ranges. The mask-weighted light curve consists of two peaks starting at $T_0-0.2$ sec, peaking at $T_0+0.7$ sec and ending at T_0+5 sec with a long tail out to T_0+200 sec with T_{90} duration (15-350 keV) of 55 ± 15 sec (Barthelmy et al. 2014; Lien et al. 2016).

We extracted the *Swift* BAT spectrum corresponding to the times of our selection for *Fermi* GBM time-averaged spectral analysis. The detailed method used for the reduction of the spectrum is as described in *Swift*-BAT software guide¹⁴. We applied energy correction using `bateconvert` to ensures that the PHA to PI energy conversion is quadratic. We used `batbinevt` to create the BAT spectrum after producing DPI, correcting for hot pixels, and mask-weighting. Further, `batphasyserr` and `batupdatephakw` are used for compensating the residuals in the response matrix and to ensure the location of GRB 140102A in instrument coordinates. In order to model the BAT spectrum, we built a detector response matrix (DRM) using tool `batdrmggen`. We modelled the BAT spectrum using the XSPEC software. We used χ^2 statistic to model the spectrum and to find the best-fit model of several different models. The time-averaged spectrum from $T_0-0.148$ sec to $T_0+131.22$ sec is best fitted by a simple power-law model with photon index (Γ_{BAT}) of 1.37 ± 0.04 (Barthelmy et al. 2014; Lien et al. 2016).

2.1.4 Joint *Fermi* and *Swift* spectral analysis

We performed a joint spectral analysis of *Fermi* and *Swift* BAT data using the Multi-Mission Maximum Likelihood framework (Vianello et al. 2015, 3ML¹⁵) version 2.3.1 software to constrain the properties of the emission mechanism of GRB 140102A. We extracted the time-averaged *Fermi*-GBM, LAT, and *Swift* BAT spectrum for a duration of T_0 to $T_0 + 5$ sec for the joint spectral analysis. We modelled the time-averaged joint spectrum with Band function and explored various other models such as Black Body along with Band function to search for thermal component in the burst; a power-law with two breaks (`bkn2pow`), and a smoothly broken power-law (SBPL) or their combinations based upon residuals of the data. We calculated Bayesian information criteria (BIC; Kass & Raftery 1995), Akaike information criterion (AIC), and Log (likelihood) for each model to find the best-fit model. We consider GBM spectrum over the energy range of 8-900 keV (NaI detectors) and 200-30000 keV (BGO detectors) for spectral analysis. However, we ignore the K-edge (33–37 keV) energy range for the analysis of NaI data. We consider 100 MeV-300 GeV energy channels for the *Fermi* LAT observations.

The best-fit spectral parameters of the joint analysis are presented in appendix A. We found that of all the six models used, the Band model with a Black Body component has the lowest BIC value. Therefore, we conclude that the time-averaged spectrum of GRB 140102A is best described with Band + Black Body function. Furthermore, time-resolved spectroscopy (see § 2.1.5) suggests that the presence of apparent BB is due to spectral evolution.

2.1.5 Time-resolved spectroscopy of GRB 140102A

Time-resolved spectroscopy is a promising tool to investigate the radiation mechanisms (non-thermal synchrotron or thermal photospheric model) and to study the correlations among the spectral parameters of GRBs, which are still an unsolved problem of the prompt emission (Zhang 2011). Initially, we resolved the main emission interval so that each extracted spectrum had a signal-to-noise ratio (SNR) equal to 25 using *Fermi* GBM data and model each spectrum with Band function only. We notice a strong correlation of α_{pt} and E_p with flux. Further, we resolved the total emission interval of GRB 140102A based on the Bayesian Block algorithm integrated over the 8-900 keV in the detector with a maximum count rate (NaI 9) and jointly analyzed *Fermi* GBM and *Swift* BAT data as the Bayesian Block algorithm is the most suitable method to identify the intrinsic intensity change in the prompt emission light curve (Scargle et al. 2013; Burgess 2014). This resulted in 17 spectra, however, two bins do not have sufficient counts to be modeled. We adopted the various models (Band, Black Body, and Cutoff-power law or their combinations) for time-resolved spectral analysis. We find that most of the temporal bins are well described with the Band function only. The best-fit parameters and their associated errors are listed in appendix A. The evolution of spectral parameters along with the light curve is shown in Figure 3. As can be seen from Figure 3, the value of E_p is changing throughout the burst resulting in spectral evolution. The E_p evolution shows an intensity-tracking trend throughout the emission. Similarly, the evolution of α_{pt} also follows an intensity-tracking trend for the first episode, whereas this tracking behavior is less clear during the second peak, and it exceeds the line of death for synchrotron slow cooling (Goldstein et al. 2013;

¹¹ <https://heasarc.gsfc.nasa.gov/W3Browse/fermi/fermille.html>

¹² https://www.swift.ac.uk/swift_portal/

¹³ <https://heasarc.gsfc.nasa.gov/FTP/caldb/>

¹⁴ https://swift.gsfc.nasa.gov/analysis/bat_swguide_v6_3.pdf

¹⁵ <https://three.ml.readthedocs.io/en/latest/>

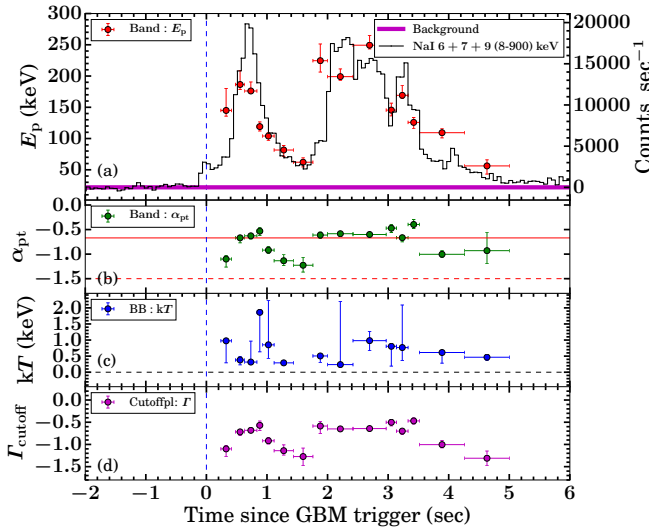


Figure 3. Evolution of spectral parameters obtained for GRB 140102A: (a) The evolution of the peak energy (red circles) is overlaid on the GBM light curve (solid black line). The horizontal magenta solid line shows the background level. (b) The evolution of the low energy spectral index using the joint *Fermi* GBM and *Swift* BAT data. The two horizontal lines are lines of death for synchrotron fast cooling ($\alpha_{pt} = -3/2$, dotted red line), and synchrotron slow cooling ($\alpha_{pt} = -2/3$, red solid line). (c) The evolution of kT (keV) obtained from the BBlack Body component. The horizontal black dashed line shows $kT = 0$ keV. (d) Evolution of photon indices for the Cutoff-power law model. Binning has been performed based on the Bayesian Block algorithm.

Chand et al. 2018) in most of the bins of the second episode, therefore the emission of the second episode may have a non-synchrotron origin. The light curve of this burst has a complicated structure and consists of two emission episodes, each of them consist of several overlapped pulses: the first episode consists of at least one pulse, and the second episode consists of at least three pulses (see Figure 3 (a)). The superposition effect, suggested in Minaev et al. (2014), could lead to intensity tracking behavior of the spectral evolution.

2.2 *Swift* XRT observations

The X-ray Telescope (XRT; Burrows et al. 2005) began observing the field of GRB 140102A on January 02, 2014 at 21:18:34.3 UT, 56.8 sec after the BAT trigger. The XRT detected a bright, uncat-alogued X-ray source located RA, and DEC = 211.9190, 1.3333 degrees (J2000) with an uncertainty of $4.8''$ (radius, 90 % containment). This location is $61''$ from the BAT onboard position but within the BAT error circle (Hagen et al. 2014). In total, there are 9.5 ks of XRT data for GRB 140102A, from 47 sec to 205 ks after the BAT trigger. The data comprise ~ 2.2 ks in Windowed Timing (WT) mode (the first ~ 8 sec were taken while *Swift* was slewing) with the remainder in Photon Counting (PC) mode. In this paper, we used X-ray data products (both light curve and spectrum) available on the *Swift* online repository¹⁶ hosted by the University of Leicester (Evans et al. 2007, 2009).

We modelled the X-ray light curve using a simple power-law function, and broken power-law model (BPL). We find that the XRT

light curve could be best described with a broken power-law model (see § 3.2.2). We calculated $\alpha_{x1} = -1.09^{+0.01}_{-0.01}$, $\alpha_{x2} = -1.50^{+0.02}_{-0.02}$, and $t_{bx} = 1298^{+108}_{-74}$ sec, where α_{x1} is the temporal index before break (t_{bx}), and α_{x2} corresponds to the temporal index after break. All the temporal parameters are also listed in Table 2.

We analyzed the *Swift* XRT spectra using the XSPEC package using an absorbed power-law model in 0.3-10 keV energy channels. The absorption includes photoelectric absorption from our Galaxy and the host galaxy of the GRB using the XSPEC components phabs and zphabs together with the source spectral model. We considered the Galactic hydrogen column density fixed at $N_{H, Gal} = 3.04 \times 10^{20} \text{ cm}^{-2}$ (Willingale et al. 2013), and a free intrinsic hydrogen column density located at the host redshift ($N_{H, z}$). The XRT spectra were grouped with a minimum of 1 count per bin unless mentioned otherwise. The statistics C-Stat is used for optimization and testing the various models. The redshift of the second absorption component was fixed at 2.02 as discussed in § 2.5.1. We also search for an additional thermal (Black Body) and other possible components in the early time WT mode spectra (63-200 sec), but we did not find any signature of thermal component based on the BIC value comparison obtained for simple absorption power-law model. All the spectral parameters for the absorbed power-law model have been listed in Table 3.

Initially, we created two time-sliced spectra (before and after the break time) using the UK Swift Science Data Centre webpages¹⁷ and found spectral decay index $\beta_{x1} = 0.56^{+0.02}_{-0.02}$ (before break) and $\beta_{x2} = 0.67^{+0.06}_{-0.06}$ (after break). Further, we created three more time-sliced spectra, using data between 63-200 sec, 200-2200 sec, and 5600- 2×10^5 sec to observed the evolution of decay slope in the X-ray band (β_x). We notice, β_x evolves and increases continuously in each temporal bins. However, the photon index obtained from the Swift Burst Analyser webpage¹⁸ could be fitted with a constant (CONS) model¹⁹, and at very late times the photon index is different and seems to have dropped (see Figure 5 (c)). We observed a late time ($\sim 4.7 \times 10^4$ to $\sim 9.3 \times 10^4$ sec) re-brightening activity in the unabsorbed X-ray flux light curve (at 10 keV).

2.3 UV/Optical Observations

Ultra-violet and optical observations were carried out using *Swift*-UVOT, BOOTES robotic, and 1.3m DFOT telescopes as a part of the present work. Details of these observations are given below in respective sub-sections. Multi-band light curves obtained from these observations are presented in Figure 4.

2.3.1 *Swift* Ultra-Violet and Optical Telescope

The *Swift* UVOT began observing the field of GRB 140102A 65 sec after the BAT trigger (Hagen et al. 2014). The afterglow was detected in 5 UVOT filters. UVOT observations were obtained in both image and event modes. Before extracting count rates from the event lists, the astrometric corrections were refined following the methodology described in Oates et al. (2009). For both the event and image mode data, the source counts were extracted using a

¹⁷ https://www.swift.ac.uk/xrt_spectra/addspec.php?target=00582760

¹⁸ https://www.swift.ac.uk/burst_analyser/00582760/

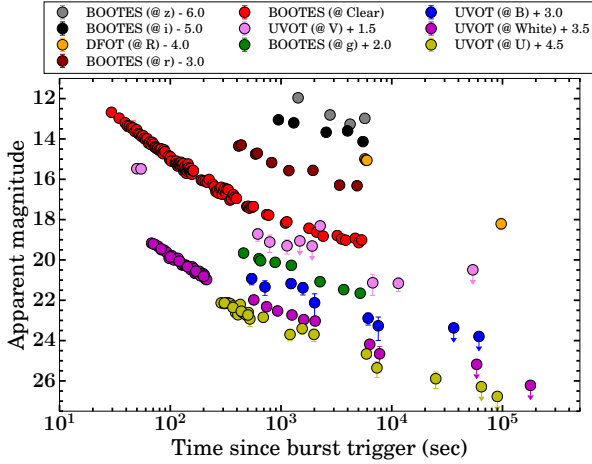
¹⁹ <https://www.ira.inaf.it/Computing/manuals/xanadu/xronos/node93.html>

²¹ https://www.swift.ac.uk/burst_analyser/00582760/

¹⁶ <https://www.swift.ac.uk/>

Table 2. The best fit models to the X-ray, combined optical light curves, and individual optical filters.

Wavelength	Model	α_1	α_2 or α_{x1}	t_{break} or t_{bx} (sec)	α_3 or α_{x2}	χ^2/dof
X-ray	broken power-law	—	-1.09 ± 0.01	1298^{+108}_{-74}	-1.50 ± 0.02	575/543
Optical/IR	power + broken power	-1.72 ± 0.04	-0.47 ± 0.03	6160^{+740}_{-240}	-1.11 ± 0.15	109/33
BOOTES Clear	2x power-law	-1.72 ± 0.04	-0.41 ± 0.04	—	—	199/104
UVOT <i>white</i>	2x power-law	$-2.19^{+0.27}_{-0.41}$	-0.86 ± 0.07	—	—	41/48
BOOTES Clear	Broken power-law	—	-1.49 ± 0.01	475 ± 15	-0.70 ± 0.01	315/106
UVOT <i>white</i>	Broken power-law	—	-1.49 ± 0.05	294 ± 58	-0.88 ± 0.07	43/48

**Figure 4. Multi-band optical light curve:** Multi-band light curves of the afterglow of GRB 140102A using UVOT, BOOTES, and Devasthal fast optical telescope (DFOT) data as a part of the present analysis as tabulated in appendix A. Magnitudes are not corrected for the extinctions.**Table 3.** The best-fit values of Photon indices from the X-ray afterglow spectral modelling for different temporal segments. We have frozen the host hydrogen column density, obtained from SED 3 (see § 2.5).

Time (sec)	Photon index	Mode
63-65196	1.59 ± 0.09	WT+PC
63-200	1.51 ± 0.03	WT
200-2200	1.61 ± 0.02	WT
$5600-2 \times 10^5$	1.63 ± 0.09	PC

region of 3" radius. In order to be consistent with the *Swift* UVOT calibration, the count rates were then corrected to 5" using the curve of growth contained in the calibration files using standard methods. Background counts were estimated using a circular region of radius 20" from a blank area of sky situated near the source position. The count rates were obtained from the event and image lists using the *Swift* standard tools `uvotevt1c` and `uvotsource`, respectively²². Later, these counts were converted to magnitudes using the UVOT photometric zero points (Breeveld et al. 2011). The UVOT data for this burst is provided in appendix A. As with data from all the following telescopes, the resulting afterglow photometry is given in AB magnitudes and not corrected for Galactic reddening of $E(B-V) = 0.03$ (Schlafly & Finkbeiner 2011).

2.3.2 BOOTES Robotic Telescope Network

The BOOTES-4/MET robotic telescope in Lijiang, China (Castro-Tirado et al. 2012) automatically responded to the BAT trigger (Hagen et al. 2014) with observations starting at 21:18:05 UT on January 02, 2014, 28 sec after the trigger. For the first 5 minutes, observations were taken with a series of 0.5 sec clear filter exposures, after which observations were taken with a systematic increase in exposure. Starting from ~ 6 minutes after the trigger, observations were also performed in rotation with the *g*, *r*, *i*, *Z*, and *Y* filters. The images were dark-subtracted and flat-fielded using custom IRAF routines. The aperture photometry was extracted using the standard IRAF software and field calibration was conducted using the SDSS DR12 catalogue Alam et al. (2015). Color transforms of Hewett et al. (2006) were used when calibrating the *Z* and *Y* filters. The BOOTES data is provided in appendix A.

2.3.3 1.3m ARIES Telescope

The 1.3m DFOT at ARIES, Nainital started observing the field of GRB 140102A ~ 1.5 hours after the trigger. Several frames in *V*, *R_c* and *I_c* pass-bands were obtained in clear sky conditions. Images were dark-subtracted, but not flat fielded since there were no available flats taken on the same night and flat fielding using those taken on a different night made the science images worse. Aperture photometry was extracted using the standard IRAF software, and field calibration was conducted using the SDSS DR12 catalogue Alam et al. (2015) and the color transforms of Robert Lupton in the SDSS online documentation²³. The optical data using the 1.3m DFOT telescope along with other data sets are provided in appendix A.

2.4 Combined Optical Light curve

In order to maximize the SNR of the optical light curves, we followed the methodology of Oates et al. (2009) to combine the individual filter light curves into one single filter (Schady et al. 2010; Kann et al. 2010; Oates et al. 2012; Roming et al. 2017; Hu et al. 2019). First, the ground-based photometry was converted from magnitudes to count rate using an arbitrary zero-point. The light curves from the different filters were then normalized to the *r* filter. The normalization was determined by fitting a power-law to each of the light curves in a given time range simultaneously. The power-law indices were constrained to be the same for all the filters, and the normalizations were allowed to vary between the filters. For the light curve of GRB 140102A, the power-law was fitted between 600-6000 sec since this is the epoch which maximized the number of filters, and the behavior in each filter appeared to be similar.

²² <https://www.swift.ac.uk/analysis/uvot/>

²³ <http://www.sdss.org/dr12/algorithms/sdssUBVRITransform/#Lupton2005>

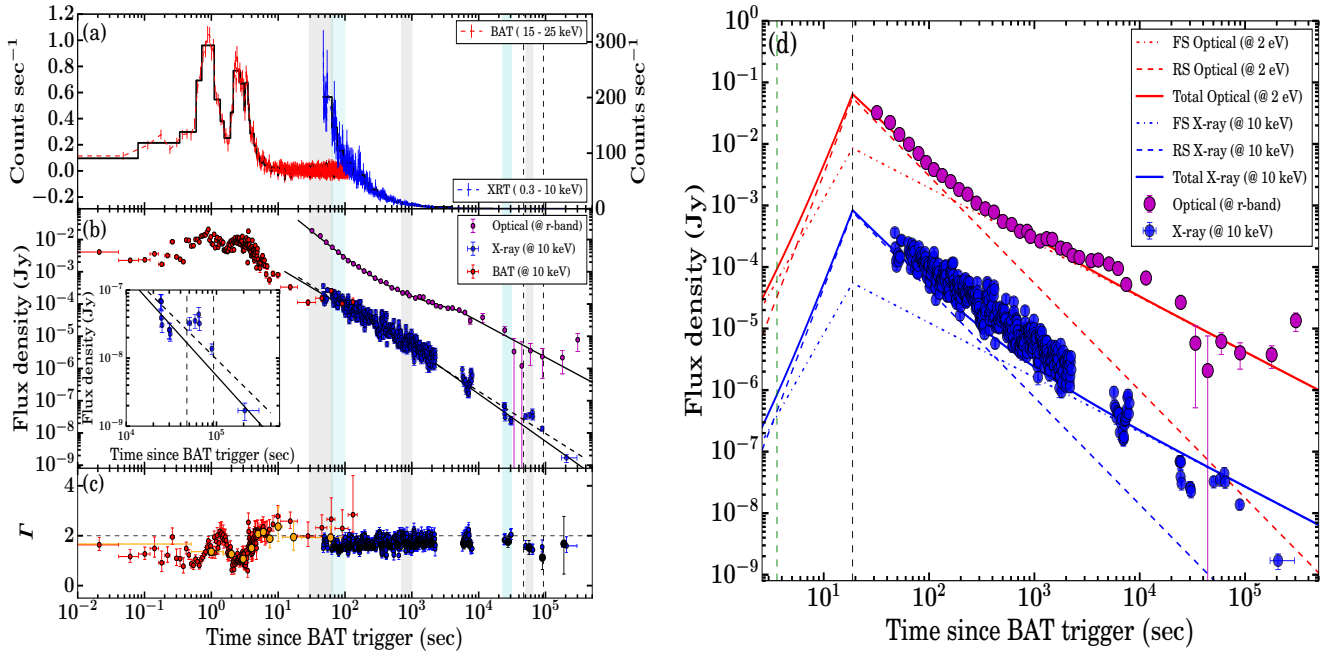


Figure 5. Multiwavelength light curve of GRB 140102A: (a) Count rate BAT and XRT light curves overlaid with the Bayesian Block analysis. (b) The X-ray and optical/UV afterglow light curves of GRB 140102A overlaid with the best-fit models: a broken power-law (X-ray, solid black line) or simple power-law (X-ray, black dashed line) or its combinations (optical, black solid line). The inset plot shows the late re-brightening activity in the X-ray light curve. (c) Evolution of photon indices within the BAT (red) and XRT (blue) window²¹. The orange and black circles indicate the evolution of BAT and XRT photon indices obtained using our spectral analysis of Bayesian Blocks bins. The shaded vertical grey and cyan color bars represent the epochs used to create the spectral energy distributions (SEDs) of GRB 140102A afterglow. The vertical dashed lines indicate the late re-brightening activity in the X-ray light curve (at 10 keV). (d) A combined forward and reverse shock model is used for the interpretation of the optical emission from GRB 140102A. The peak flux is obtained at the crossing time $t_x = 18.79$ sec and for $t > t_x$ power-law behavior of the afterglow model is followed. The optical flux is explained using the sum of reverse and forward shock components. The same set of parameters produce a lower amount of early X-ray flux in this model. The vertical green and black dashed lines indicate the end time of T_{90} duration and deceleration time, respectively. The model parameters are given in Table 5.

However, the normalization led to a slight offset between the UVOT *white* and *V* band data in comparison to the BOOTES-clear filter. We will discuss the consequences on model fitting in § 3.2.3. After the light curves were normalized, they were binned by taking the weighted average of the normalized count rates in time bins of $\Delta T/T = 0.2$. The combined optical light curve is shown in Figure 5.

2.5 Spectral Energy Distributions

SEDs were produced at five epochs (29-65 sec, 63-100 sec, 700-1000 sec, 23-31 ks, and 51-65 ks) following the prescription within De Pasquale et al. (2007), which is based on the methodology of Schady et al. (2007). We used XSPEC (Arnaud 1996) to fit the optical and X-ray data. We adopted two models, a simple power-law model and a broken-power law model. The difference between the indices of the broken power-law model was fixed at 0.5, consistent with the expectation of a synchrotron cooling break (see § 3.2.3, Zhang & Mészáros 2004). In each model, we include a Galactic and intrinsic absorber using the XSPEC models *phabs* and *zphabs*. The Galactic absorption is fixed to $N_{\text{H,Gal}} = 3.04 \times 10^{20} \text{ cm}^{-2}$ (Willingale et al. 2013). We also include Galactic and intrinsic dust components using the XSPEC model *zdst*, one at redshift $z=0$, and the other is free to vary. The Galactic reddening was fixed at $E(B-V)=0.0295$ according to the map of Schlafly & Finkbeiner (2011). For the extinction at the redshift of the burst, we test Milky

Way, Large and Small Magellanic Clouds (MW, LMC and SMC) extinction laws (Pei 1992). All the five SEDs are shown in Figure 6. We extrapolated the best-fit model towards the LAT frequencies to search for a possible spectral break between X-ray and GeV. All the results of SEDs are listed in Table 4.

2.5.1 Photometric Redshift

A spectroscopic redshift for the GRB was not reported and could not be determined from GTC spectroscopic observations of the host galaxy (see § 2.6). To determine a photometric redshift, we, therefore, created a SED using the afterglow data (X-ray and Optical) between 700 sec and 1000 sec. During this time, there is no break in the X-ray light curve, also, no spectral evolution is observed. The evolution of the X-ray photon index (Γ_{XRT}) measured during this time window is consistent with not changing (see Figure 5). Using the methodology outlined in § 2.5, we fit the SED with the simplest model, a power-law, which we find to be statistically unacceptable with χ^2 for the LMC and SMC 282 and 316 respectively for 213 degrees of freedom. However, for the MW model, we find a better χ^2 (223) for the same number of degrees of freedom. Further, we fit the SED with the broken power-law model. For the MW, LMC, and SMC, all the fits are statistically acceptable with χ^2 of 169, 178, 185, respectively for 212 degrees of freedom. We notice that for this SED (700-1000 sec), the MW model both for power-law and broken power-law fit show the smallest reduced χ^2 , however, the

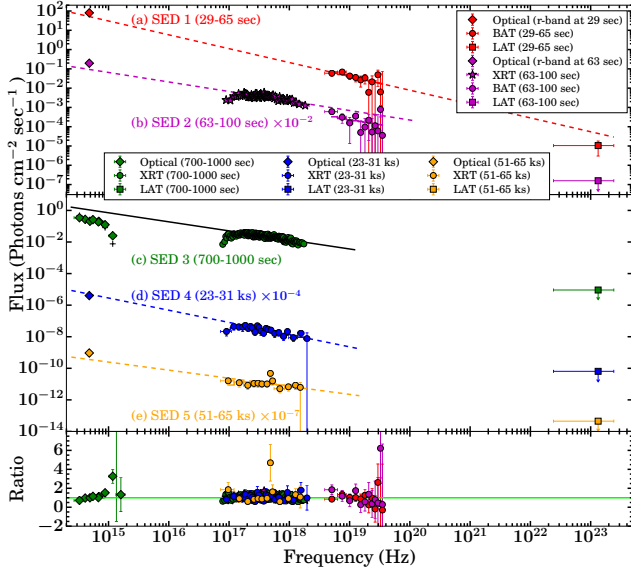


Figure 6. Spectral energy distributions: (a) SED 1 at 29-65 sec, the black dashed lines show the extrapolations of the power-law fit to the BAT spectra to the optical and LAT frequencies. The observed LAT flux is lower than the extrapolated value, and it indicates a presence of possible spectral break between BAT and LAT frequencies. (b) SED 2 at 63-100 sec, the black dashed lines show the extrapolations of the unabsorbed power-law model to the optical frequencies. (c) SED 3 at 700-1000 sec, used to constrain the redshift of the burst. The solid black line is the best-fit by a simple power-law from the joint X-ray and Optical spectral fit. (d) SED 4 23-31 ks. (e) SED 5 51-65 ks. The bottom panel shows the ratio of data to the model. The horizontal lime green solid line corresponds to the ratio equal to 1.

Table 4. The best fit results of optical and X-ray spectral indices at different epoch SEDs and their best describe spectral regime. p is the mean value of the electron distribution indices calculated from observed value of $\alpha_{\text{opt}}/\alpha_{\text{x-ray}}$ and $\beta_{\text{opt}}/\beta_{\text{x-ray}}$ of best describe spectral regime.

SED	Time interval (sec)	$\beta_{\text{x-ray/opt}}$	p (Spectral regime)	χ^2_r
1	29-65	$0.72^{+0.45}_{-0.42}$	2.33 ± 0.21 ($\nu_{\text{opt}} < \nu_{\text{x-ray}} < \nu_c$)	0.88
2	63-100	$0.49^{+0.05}_{-0.05}$	2.10 ± 0.21 ($\nu_{\text{opt}} < \nu_{\text{x-ray}} < \nu_c$)	1.01
3	700-1000	$0.57^{+0.02}_{-0.02}$	2.09 ± 0.29 ($\nu_{\text{opt}} < \nu_{\text{x-ray}} < \nu_c$)	1.05
4	23000-31000	$0.77^{+0.22}_{-0.22}$	2.64 ± 0.21 ($\nu_{\text{opt}} < \nu_{\text{x-ray}} < \nu_c$)	0.78
5	51000-65000	$0.51^{+0.32}_{-0.32}$	2.38 ± 0.40 ($\nu_{\text{opt}} < \nu_{\text{x-ray}} < \nu_c$)	1.27

We calculated NH_2 ($0.61^{+0.11}_{-0.10} \times 10^{22} \text{ cm}^{-2}$), host extinction ($0.21^{+0.02}_{-0.02} \text{ mag}$) and redshift ($2.02^{+0.05}_{-0.05}$) using the SED 3. χ^2_r notify the reduced chi-square values for SEDs at different epochs. Uncertainty in the calculation of p is obtained with a confidence level of 95 %.

reduced χ^2 is less than 1 for broken power-law fit indicating that the model is "over-fitting". In the case of power-law model, the reduced χ^2 is close to one. It confirms that the power-law model is the best fit. The redshift values for all three extinction laws are similar and consistent within 3σ . Taking the redshift from the MW model, we find a photometric redshift of $2.02^{+0.05}_{-0.05}$ for GRB 140102A. We adopted this value for all our subsequent analyses.

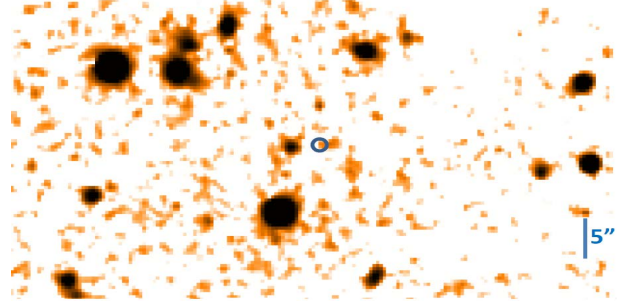


Figure 7. H-band observations of the host galaxy of GRB 140102A using 3.5m CAHA telescope. The blue circle marks the afterglow position. North is up and East to the left.

2.6 Host Galaxy Observations

2.6.1 10.4m GTC telescope

The 10.4m Gran Telescopio Canarias (GTC; Canary Island, Spain) obtained photometry for the host galaxy on the 18th July 2017. Images in the g,r,i,z filters were obtained using the Optical System for Imaging and Low-Intermediate Resolution Imaging Spectroscopy (OSIRIS) instrument (Cepa et al. 2000). The images were dark-subtracted and flat-fielded using custom IRAF routines. Aperture photometry was performed using standard IRAF software, and field calibration was conducted using the SDSS DR12 catalogue (Alam et al. 2015). The host photometry from GTC and CAHA 3.5m telescope, described next, is given in AB magnitudes and not corrected for Galactic reddening of $E(B-V) = 0.03$ (Schlafly & Finkbeiner 2011). These values are given in appendix A.

Optical spectroscopy of GRB 140102A was obtained using the 10.4m telescope on Feb 26, 2014, and Feb 26, 2015. In both cases, the grism, which covers the 5400–10000 Å wave range was used. Unfortunately, the S/N on the extracted spectra was very low, and we did not detect any emission features. At the photometric redshift, we would not expect any host galaxy emissions in this wavelength range.

2.6.2 3.5m CAHA telescope

The 3.5m telescope at Calar Alto Astronomical Observatory (CAHA) observed the field of GRB 140102A on the 13th May 2014, 4 months after the trigger. A series of 59 H band images were taken, each with 65 sec exposure and, after dark-subtraction and flat-fielding using custom IRAF routines, were median combined to create a single image (see Figure 7). Aperture photometry was performed using standard IRAF software, and field calibration was conducted using the 2MASS catalogue (Skrutskie et al. 2006).

2.6.3 3.6m DOT telescope

We observed the host galaxy of GRB 140102A using the 4Kx4K CCD Imager (Pandey et al. 2017) mounted at the axial port of the 3.6m Devasthal Optical Telescope (DOT) of ARIES Nainital on 16th January 2021 ~ seven years after GRB detection. Observations were carried out in the R filter with a total exposure time of 45 minutes ($3 \times 300 \text{ sec}$ and $2 \times 900 \text{ sec}$). We performed the reduction of data using IRAF packages. After pre-processing, we stacked the images to create a single image and perform the aperture photometry. More details about the reduction method can be found in Kumar et al. (2021). We did not detect the host galaxy in the R -band. We

calculated the 3 sigma limiting magnitude value equal to 24.10 mag (AB), calibrated with the nearby USNO-B1.0 field.

3 RESULTS

Based on the multi-band observations obtained from various space and ground-based facilities of GRB 140102A, we discuss the results based on the present analysis of both prompt emission and afterglows, including the host galaxy observations.

3.1 Prompt emission

In the present subsection, we show the results of the prompt emission properties of GRB 140102A and their comparison with other well-studied GRBs samples.

3.1.1 Spectral Hardness, Variability Time scale and Spectral lag

We calculated the time-integrated HR by dividing the counts in 10 - 50 keV and 50 - 300, keV energy bands for the 6th + 7th + 9th NaI detectors (see Table 1) to make a comparison with other *Fermi* GRBs published in Goldstein et al. (2017). We calculated T_{90} durations of GRB 140102A considering the total emission episodes using GBM data. Our result for the T_{90} calculation (see Table 1) is consistent with Zhang & Bhat (2014) and its value lies in the overlapping interval of the bi-modal duration distribution of GRBs. The error in T_{90} is calculated by simulating 10,000 light curves by adding a Poissonian noise with the mean values at observed errors (Minaev et al. 2014; Narayana Bhat et al. 2016). In Figure 8 (a), we show the HR- T_{90} diagram of GRB 140102A. The probabilities of a GRB classified as a short or long GRB from the Gaussian mixture model in the logarithmic scale are also shown in the background (taken from Goldstein et al. 2017).

Minimum variability time scale (MacLachlan et al. 2013, t_{mvts}) is important to constrain the source emission radius (R_c) of the source (Golkhou et al. 2015). We calculated the t_{mvts} of GRB 140102A using continuous wavelet transforms²⁴ discussed in Vianello et al. (2018) and found $t_{\text{mvts}} \sim 0.2$ sec for this burst. In Figure 8 (b), we show GRB 140102A in t_{mvts} - T_{90} distribution plane along with the sample of SGRBs and LGRBs studied by (Golkhou et al. 2015). Further, we calculated R_c (see equation 1) using the following relation obtained from Golkhou et al. (2015).

$$R_c \simeq 7.3 \times 10^{13} \left(\frac{L_{\gamma, \text{iso}}}{10^{51} \text{ erg/sec}} \right)^{2/5} \left(\frac{t_{\text{mvts}}/0.1 \text{ sec}}{1+z} \right)^{3/5} \text{ cm.} \quad (1)$$

We estimated the source emission radius (R_c) $\simeq 4.9 \times 10^{14}$ cm for GRB 140102A.

For most of the LGRBs, time lags, also known as spectral lags, often appear in light curves among different energy bands (Wei et al. 2017). The spectral lag is generally interpreted due to the spectral evolution (Peng et al. 2011; Shao et al. 2017). We calculated the time lags of light curves among different energy bands using the cross-correlation function ((CCF); Norris et al. 2000; Ukwatta et al. 2010) from T_0 to $T_0 + 5.0$ sec, following the method described in Zhang et al. (2012). We found negative lag values for GRB 140102A, which indicates that higher energy

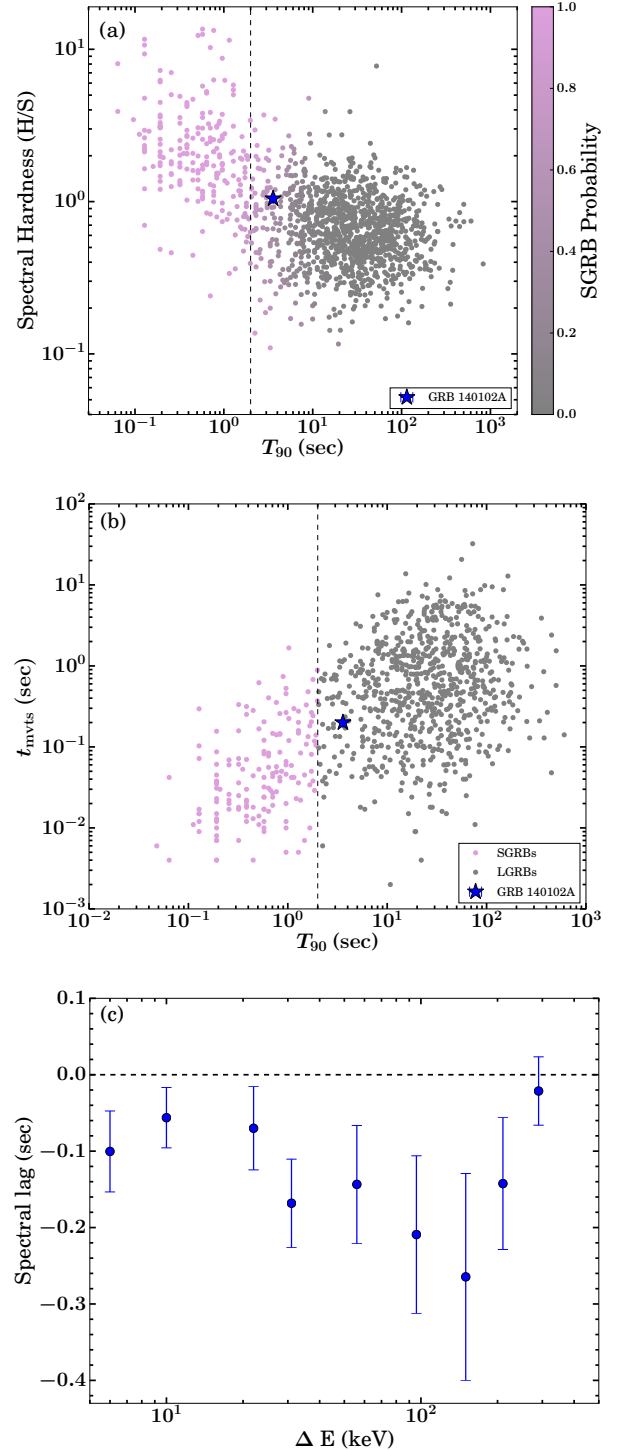


Figure 8. Prompt emission properties of GRB 140102A (a) The spectral hardness and T_{90} for GRB 140102A (shown with a blue star) along with the data points for short and long GRBs used in Goldstein et al. (2017). The left side color scale shows the probability of a GRB belonging to SGRBs class. The vertical dashed lines show the boundary between SGRBs and LGRBs. (b) GRB 140102A (shown with a blue star) in T_{90} vs. minimum variability time scale (t_{mvts}) plane along with the LGRBs and SGRBs sample studied by Golkhou et al. (2015). (c) Spectral lag as a function of energy for GRB 140102A using the GBM multi-channel light curves. The negative lag value shows that higher energy photons arrived later than the lower energy photons. The black dashed line shows the zero lag.

²⁴ <https://github.com/giacomov/mvts>

photons arrived later than the lower energy photons. Negative lag could be connected with superposition effect, described in Minaev et al. (2014). The analysis of spectral lag for GRB 140102A is shown in Figure 8 (c).

3.1.2 Correlations between Spectral parameters

In the present section, we discussed the correlations between spectral parameters obtained from time-resolved spectral analysis. These correlations play an important role in probing the emission mechanisms of GRBs during the prompt emission phase. Initially, we examine the correlation between E_p -flux, α_{pt} -flux, and E_p - α_{pt} using the Band function based on GBM data only for each bin obtained from the SNR binning method. We found a strong correlation between the E_p of the Band function and the flux in 8-900 keV energy ranges with a Pearson coefficient (r) and p-value of 0.86 and 1.88×10^{-5} . We also found a strong correlation between α_{pt} of Band function and flux with r and p-value of 0.75 and 7.4×10^{-4} . As E_p and α_{pt} show a strong correlation with flux, we investigated the correlation between E_p and α_{pt} . A moderate correlation with r and p-value of 0.67 and 4.3×10^{-3} respectively. We also performed the time-resolved spectral analysis of *Swift* BAT data and find a strong correlation between BAT photon indices (Γ_{BAT}) and the fluxes in 15-350 keV energy ranges with r and p-value of 0.86 and 1.02×10^{-13} . Furthermore, we jointly model the GBM and BAT spectrum of each bins obtained from Bayesian Block method to cross check the correlation results and we still find a strong correlation between the E_p and flux with Pearson coefficient (r) and p-value of 0.79 and 4.8×10^{-4} . However, we notice moderate correlation between α_{pt} and flux with r and p-value of 0.65 and 8.6×10^{-3} . E_p and α_{pt} also show moderate correlation with r and p-value of 0.61 and 1.7×10^{-2} . Therefore, GRB 140102A has the characteristics of a ‘double-tracking’ GRB (Both the low-energy spectral index and the peak energy follow the intensity-tracking pattern) similar to GRB 131231A (Li et al. 2019). The spectral parameters α_{pt} , E_p for GRB 140102A are correlated with the observed flux, and we have shown this in Figure 9. Our result is consistent with Duan & Wang (2020), where they performed the spectral analysis of Fermi LLE GRBs including GRB 140102A using the Fermi GBM data only; they have used RMFIT tool and χ^2 statistics for measuring the goodness of fit. In contrast, we have performed the joint *Fermi* and *Swift* spectral analysis using the Bayesian spectral fitting package 3ML, which is a more appropriate method. Ryde et al. (2019) also studied the correlation between the energy flux and α_{pt} , for a sample of the 38 *Fermi* GBM detected bursts having individual pulse structures. They found significant correlations in most pulses similar to the case of GRB 140102A.

3.1.3 Amati and Yonetoku correlations

We study two well known prompt emission correlations for GRB 140102A. The first one is Amati correlation (Amati 2006; Fana Dirirsa et al. 2019), which is the correlation between spectral peak energy (see Table 1) corrected to the rest frame ($E_{p,z}$) and isotropic equivalent γ -ray energy ($E_{\gamma,iso}$), and the second one is Yonetoku correlation (Yonetoku et al. 2004), which is a correlation between $E_{p,z}$ and isotropic peak luminosity ($L_{\gamma,iso}$) in the cosmological rest frame ($z = 2.02$). We estimated the time-integrated (T_0 to $T_0 + 5.0$ sec) total fluence in 1-10⁴ keV energy band for $E_{\gamma,iso}$ calculation. We placed GRB 140102A on the Amati correlation plane along with the data points for LGRBs and SGRBs published

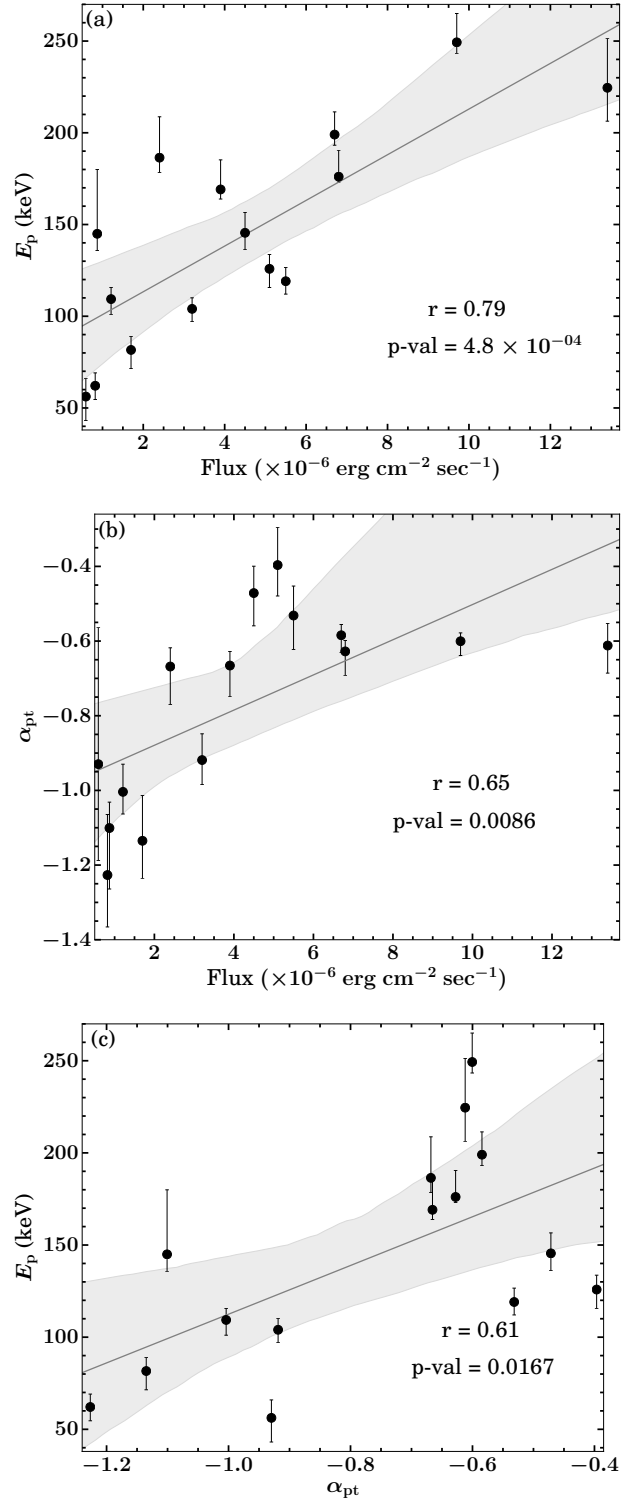


Figure 9. Correlations between spectral model parameters : (a) Peak energy versus flux, (b) low-energy spectral index versus flux, (c) Peak energy versus low-energy spectral index. Correlation shown in (a), (b), and (c) are obtained using joint *Fermi* GBM and *Swift* BAT observations and modelling with Band function. The best-fit lines are shown with solid grey lines, and the shaded grey region shows the 2σ confidence interval of the correlations.

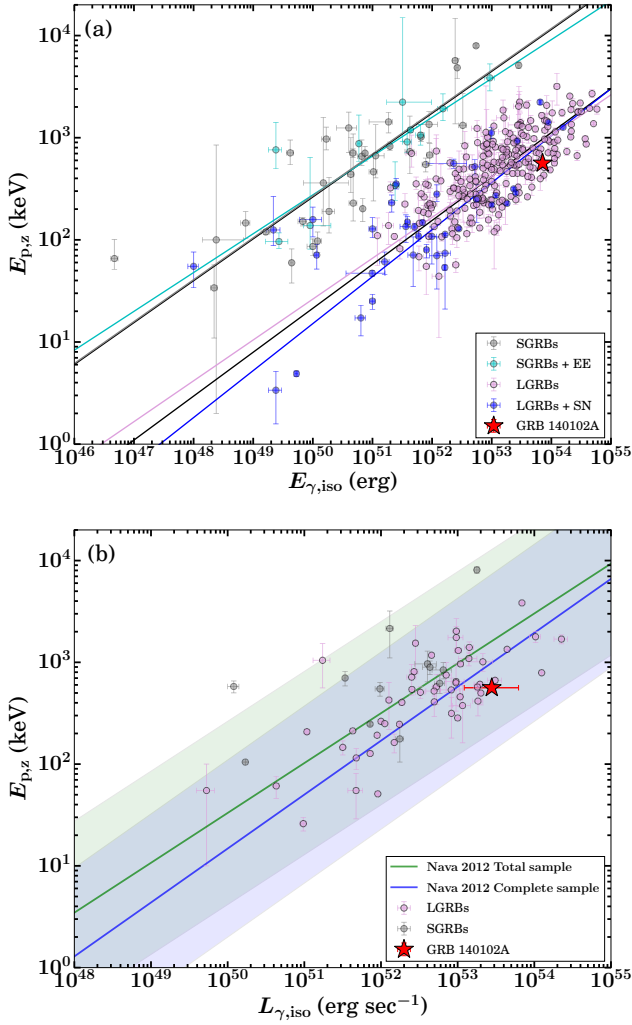


Figure 10. Amati and Yonetoku correlation plane for GRB 140102A: (a) GRB 140102A in the Amati correlation plane along with other the data points published in [Minaev & Pozanenko \(2020\)](#). Various colored lines correspond to the best-fit lines for different classes mentioned in the legend. (b) GRB 140102A in the Yonetoku correlation plane along with GRBs sample published in [Nava et al. \(2012\)](#). The colored lines show the best-fit and shaded region represents the 3σ scatter of the correlation.

in [Minaev & Pozanenko \(2020\)](#) and found that GRB 140102A is consistent with the Amati correlation of LGRBs (see Figure 10 (a)). In Yonetoku correlation plane, GRB 140102A lies within the 3σ scatter of total and complete samples of GRBs (see Figure 10 (b)) studied by [Nava et al. \(2012\)](#).

3.2 Multi-wavelength Afterglow

In this subsection, we present the afterglow properties of GRB 140102A.

3.2.1 Soft tail emission

The observed soft tail emission from GRBs is useful to constrain the transition time from prompt emission to afterglow phase ([Sakamoto et al. 2007](#)). *Swift* BAT observed the soft emission from

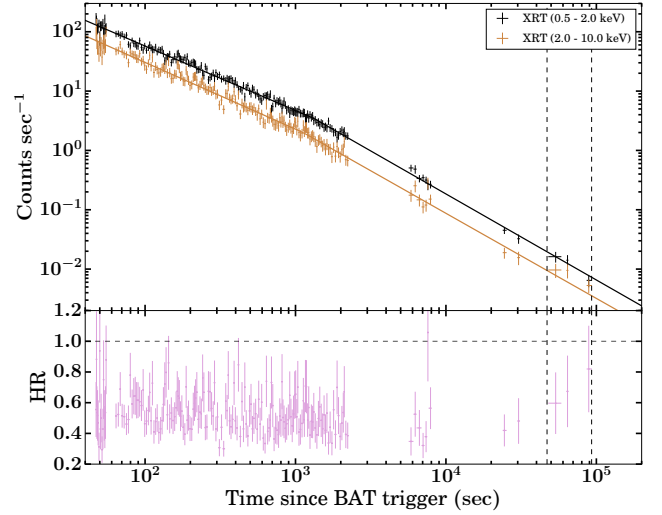


Figure 11. The X-ray count rate light curves in soft (0.5-2.0 keV) and hard (2.0-10.0 keV) energy channels. The solid lines show the best-fit (broken power-law model) line to both the light curves. The bottom panel shows the evolution of HR in the same XRT energy bands. The vertical black dashed lines show the epoch of re-brightening activity in the X-ray light curve (at 10 keV).

GRB 140102A until ~ 200 sec. To understand the origin of this emission, we binned the BAT count-rate light curve based on Bayesian Blocks and performed the spectral analysis of each interval using `pegpwr1w` model (a simple power-law model with pegged normalization²⁵). The evolution of photon indices (black circle) calculated as mentioned above in BAT soft (15-25 keV) energy channels are shown in Figure 5 (c). Also, spectral indices constrained using SEDs at 29-65 sec and 63-100 sec indicate agreement between BAT and optical emissions (after correcting for the RS contribution, in the case of SED at 29-65 sec, the optical data point is already within the BAT power-law uncertainty region due to large uncertainty on the index as the presence of a low signal in BAT). Furthermore, We notice that BAT photon indices do not show a rapid fluctuation and are consistent with those estimated at XRT frequencies during the soft emission phase. We also use early X-ray observations to investigate the underlying tail emission. We created the XRT light curve in soft (0.5-2.0 keV) and hard (2.0-10.0 keV) energy channels and examined the evolution of HR to identify spectral evolution at early epochs (see Figure 11). We performed the temporal and spectral analysis for this early epoch (~ 47 sec to 200 sec post burst) XRT (WT mode) data. We find a temporal decay of $0.99^{+0.03}_{-0.03}$ and spectral index equal to $0.59^{+0.04}_{-0.04}$ during this epoch. These values are found to disagree with the expected closure relation for early X-ray observations to be prompt tail emission as described by [Zhang et al. \(2006\)](#) ($\alpha = 2 + \beta$). Based on the above, we suggest that soft tail emission observed from GRB 140102A had possibly afterglow origin.

²⁵ <https://heasarc.gsfc.nasa.gov/xanadu/xspec/manual/node297.html>

3.2.2 X-ray and Optical afterglow light curves

The X-ray afterglow light curve, shown in Figure 5, declines from the beginning of observations and shows no features, such as steep and shallow decays phases or any flaring activity. A fit of a power-law to the light curve gives a $\chi^2/\text{dof} = 1190/545$, suggesting a more complex model is required to fit the data. A broken power-law model is a better fit with $\chi^2/\text{dof} = 575/543$; according to the F -test, the broken power-law model gives an improvement at the $> 5\sigma$ confidence level with respect to the power-law model. We also tested to see if a further break would provide an improvement. The double broken power-law model results in $\chi^2/\text{dof} = 565/541$. The F -test suggests the additional break is not required since the improvement is only at the 2.6σ level. The best-fit model is given in Table 2.

The optical multi-band light curve is shown in Figure 4. Observations in the UVOT *white* and BOOTES-clear filters started before most of the other optical filters and have the best sampling and SNR during the first few thousand seconds. A power-law fit to both of these light curves results in $\chi^2/\text{dof} = 1754/108$ and $\chi^2/\text{dof} = 89/50$ for BOOTES-clear and UVOT *white*, respectively. Both of which are statistically unacceptable at the $> 3\sigma$ level. Since the light curves display an early steep to shallow transition, suggesting the presence of a reverse dominated shock (Gao et al. 2015) when fitting a more complex model such as a broken power-law, the sum of two power-law models, or their combinations. Both fits give slightly better values, with the broken power-law resulting in $\chi^2/\text{dof} = 315/106$ and $\chi^2/\text{dof} = 43/48$ for BOOTES-clear and UVOT *white* respectively, and for the two power-law components, we achieved $\chi^2/\text{dof} = 203/106$ and $\chi^2/\text{dof} = 43/48$. While both models fit the UVOT *white*, for the higher sampled BOOTES-clear filter, both fits are still unacceptable at $> 3\sigma$ level, although the two power-law model results in a smaller reduced χ^2 . The two power-law model appears to fit the data well, it is likely that the χ^2 is large for BOOTES-clear due to the significant scatter in the data about the best-fit model.

The BOOTES photometry ends at 6ks and in UVOT, there is an observing gap between 2ks and 5ks, after which the S/N of the light curve is poor. Therefore we created a single filter light curve by combining the optical light curves from BOOTES and UVOT in order to create a light curve with better sampling and high SNR as described in § 2.4. A broken power-law fit to this light curve results in an unacceptable $\chi^2/\text{dof} = 284/35$. We, therefore, fit the light curve with a double broken power-law. This resulted in a slightly improved $\chi^2/\text{dof} = 256/33$; the F -test suggests the addition of a break is not required since the improvement is $< 2\sigma$. However, on the basis that such a steep decay in the early optical light curve, may be due to the reverse shock, resulting in two-components producing the observed optical afterglow (Wang et al. 2015), we also tested two-component models. Firstly we tested two power-laws, which results in $\chi^2/\text{dof} = 192/35$. The fit is an improvement on the previous models but is still unacceptable. We therefore, also tried with a power-law plus broken power-law model. The fit results in a $\chi^2/\text{dof} = 109/33$ with the F -test suggesting the addition of a power-law to the broken power-law model is an improvement at 3σ confidence.

We note that when constructing the combined light curve, color evolution was observed between the BOOTES and UVOT data, with the UVOT *white* and *V* band data, during the initial steep decay, systematically lower than the BOOTES clear data. The CCD of BOOTES is sensitive to much redder photons, covering

the range 3000 Å to 11000 Å²⁶, while the UVOT *white* filter covers a wavelength range of between 1700-6500 Å and the UVOT *V* filter covers a range 5000-6000 Å. This would suggest that the spectrum during the steep decay is redder in comparison to the rest of the afterglow. After normalization, the data were group together, weighted by the errors, since the early BOOTES and UVOT data do not align well, this may affect the measurement of temporal indices. However, we see that the initial steep decay of the combined light curve is consistent with the tightly constrained steep decay measured with BOOTES-clear and the less well constrained UVOT *white*. The steep decay of the combined light curve is most similar to that of the BOOTES clear filter, as the BOOTES light curve has better SNR than the UVOT *white* filter and thus is the dominant component when creating the weighted binned light curve.

We noticed a break in the X-ray light curve at ~ 2 ks. The temporal break may be due to the change in spectral behavior or due to energy injection from the central engine, which we notice as a transition from shallow decay phase and followed by a steep decay ($1.50^{+0.02}_{-0.02}$). We sliced the X-ray light curve (count rate) into small temporal bins (see Figure 5 (a)) to study the possible origin of this break. This resulted in 20 spectra, however, five bins do not have significant counts for the spectral modelling. The evolution of photon indices is shown in Figure 5 (c, black circles). It indicates that there is no significant change in β_x (as it is expected for ν_c passing through) close to the break in the X-ray light curve. When we fitted the photon index with a constant (CONS) model, we get a very good fit, suggesting that there is no evolution. If we consider that ν_c is between the BAT and LAT frequencies as suggested from SED 1 (29-65 sec, see § 4.1), ν_c could not pass through the X-ray band, inconsistent with expectations (i. e. $t^{-0.5}$), indicating that X-ray break is not due to the spectral break. We also tested the other possibilities of the origin of this break, such as energy injection. Considering adiabatic cooling with energy injection from the central engine, the inferred value of α_x (1.08 ± 0.02) from observed β_x (0.56 ± 0.02) matches with the observed value of $\alpha_{x-\text{ray}}$ (1.09 ± 0.01) for the spectral regime $\nu_m < \nu_{x-\text{ray}} < \nu_c$ and for the slow cooling case in the ISM-like medium. We estimate the value of electron distribution index $p = 2.12 \pm 0.04$ from $p = (2\beta + 1)$. We notice that the inferred value of p is close to what we obtained from modelling. We observed an early excess X-ray flux similar to those found in many other RS dominated bursts. It could be possible to explain early X-ray excess as an energy injection episode lasting up to 2 ks. Though we did not find an achromatic break in the X-ray and optical light curves as expected due to the end of the energy injection episode (Laskar et al. 2015), however, we notice a break in the optical data ~ 6 ks (see Table 2 and Figure 5 (b)).

During the late time re-brightening phase in the unabsorbed X-ray flux light curve (at 10 keV), we notice the hardening in the photon index (see Figure 5) and in the hardness ratio (see Figure 11). This could not be explained by the frequency crossing the X-ray band as the photon index reverses back to the original position after this phase. This unusual emission could be originating due to patchy shells or a refreshed shocks (Chand et al. 2020; Hu et al. 2021).

3.2.3 Optical and X-ray afterglow light curve modelling

The fireball synchrotron model for afterglows is currently the favoured scenario in terms of producing the observed multi-

²⁶ <http://www.ando.com/scientific-cameras/ixon-emccd-camera-series/ixon-ultra-888>

wavelength emission. In this model, the afterglow is a natural consequence of the beamed ejecta ploughing through the external medium and interacting with it, producing the observed synchrotron emission. The spectral and temporal behavior of the afterglow emission could be described by several closure relations (Sari et al. 1998; Meszaros & Rees 1997; Sari & Piran 1999; Dai & Cheng 2001; Racusin et al. 2009, see the last reference for a comprehensive list). This set of relations connect the values of α and β to the power-law index of the electron energy distribution p , making it possible to estimate its value from the observations, which is typically found to be between 2 and 3 (Panaitescu & Kumar 2002; Starling et al. 2008; Curran et al. 2009); the density profile of the external medium (constant or wind-like), and the relative positions of breaks in the synchrotron spectrum, primarily the synchrotron cooling frequency ν_c and the synchrotron peak frequency ν_m . Another break frequency is called the synchrotron self-absorption frequency, though it does not influence the optical/UV or the X-rays during the timescales studied here. There are also closure relations describing temporal and spectral indices in the scenario that the afterglow is injected by an additional energy component (Zhang et al. 2006).

For jets having a single component, it is derived that the optical/UV and X-ray emissions are produced within the same region and therefore are explained by the same synchrotron spectrum, with the possibility that one or more of the break frequencies are between the two observing bands. This translates that the optical/UV and X-ray temporal indices, determined from an afterglow, should be described by closure relations that rely on the same assumptions about the ambient media, the electron energy index, p , and the energy injection parameter q .

The thin shell case ($T_{\text{dec}} > T_{90}$) Type-II features (also called flattening type, the peak of forward shock is below the reverse shock component) discussed by Gao et al. (2015) are used to interpret the optical emission. However, the forward shock emission dominates after ~ 100 sec. The optical emission in between $\sim 30 - 100$ sec follows the emission predicted by the reverse shock emission. This makes the early optical emission from this GRB a combination of RS+FS components. The RS model parameters for the early optical emission are useful to understand the magnetic energy available in the jet and the source environment (Kobayashi & Zhang 2003; Kobayashi & Sari 2000).

The reverse shock crossing time is defined as $t_x = \max(T_{\text{dec}}, T_{90})$, which is important to estimate the peak emission for reverse shock. The break frequency evolution with time is $\nu_m^r \propto t^6$ for $t < t_x$ and $\nu_m^r \propto t^{-54/35}$ for $t > t_x$, however ν_m^f is constant before crossing time and decreases with time after this as $t^{-3/2}$, where r denotes the reverse shock and f is used for forward shock (Gao et al. 2015). The cooling frequency $\nu_c^r \propto t^{-2}$ for $t < t_x$ and $\nu_c^r \propto t^{-54/35}$ after t_x . The same for forward shock is $\nu_c^f \propto t^{-2}$ for $t < t_x$ and $\nu_c^f \propto t^{-1/2}$ after crossing time. The maximum synchrotron flux is defined as $f_{\text{max}}^r \propto t^{3/2}$ for $t < t_x$ and after crossing time it decreases as $t^{-34/35}$. Similarly, $f_{\text{max}}^f \propto t^3$ for $t < t_x$ and independent of time after crossing time (Gao et al. 2015). We model the afterglow emission and the parameters obtained to explain GRB 140102A are listed in Table 5. We have used Bayesian analysis PyMultiNest software (Buchner et al. 2014) to estimate the afterglow modelling parameters and associated errors. A corner plot showing the analysis results is shown in appendix A. In the right panel of Figure 5, we have shown the optical and X-ray light curves based on afterglow modelling. The parameters electron energy index p (2.00 for RS and 2.19 for FS, respectively), micro-physical parameters ϵ_e and ϵ_B for the RS and FS are constrained using optical and X-ray data.

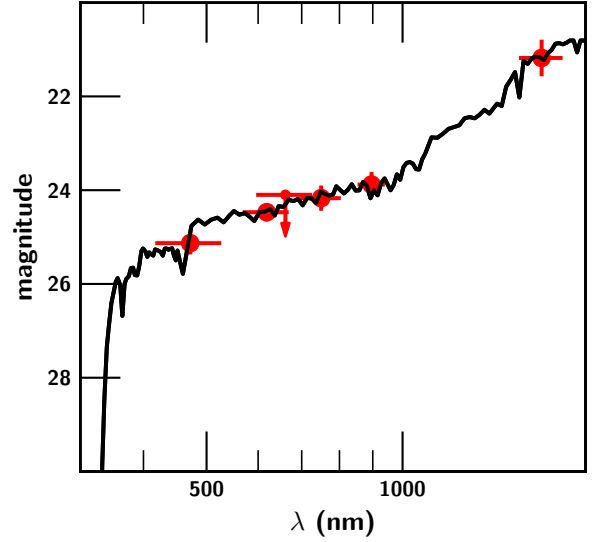


Figure 12. The SED of the host galaxy of GRB 140102A fitted by the LePhare with redshift $z=2.8^{+0.7}_{-0.9}$. Filled red circles depict respectively the data points in the filters g, r, R, i, z, H from original observations (see § 2.6 and Table A7). All magnitudes are in the AB system.

The model can explain the optical emission and produces a slightly lower X-ray flux than observed at early times (the excess can be explained in terms of energy injection, see § 3.2.2). However, in a few cases of GRBs, this kind of feature (excess X-ray emission) has been seen, and possible scenarios like (i) wavelength-dependent origin and (ii) mass loss evolution dependence are discussed by Yi et al. (2013); Xie et al. (2020).

3.3 Host Galaxy SED modelling

The host characteristics, such as morphology, stellar population, offset, etc., of LGRBs and SGRBs, are different. These characteristics are likely associated with the physical conditions required to produce GRBs. LGRBs are largely localized in active star-forming and young stellar population dwarf galaxies. On the other hand, SGRBs belong to old stellar population galaxies (Savaglio et al. 2009; Berger 2009). Therefore, host parameters can be used to constrain about progenitors and their environment (useful in such cases where T_{90} duration of burst lies in the brink regime as in the case of GRB 140102A). We calculated the offset value of 0.52 ± 0.02 arcsec (~ 4.46 kpc) between the afterglow position and the center of the host galaxy of GRB 140102A. This value is higher in comparison to the median offset value studied by Lyman et al. (2017). Recently Wang et al. (2018) studied the possible correlations between rest-frame prompt emission (T_{90} , $E_{\gamma, \text{iso}}$, and $L_{\gamma, \text{iso}}$) properties with host properties. They found that these parameters negatively correlate with offset (GRB 140102A also follows it). As we could not constrain the redshift of GRB 140102A using the spectroscopic observations of the host galaxy, we attempted the photometric observations of the host in six broad-band filters. These inspired us to perform a detailed SED modelling and compared the results with a well-studied GRBs host sample.

We used LePhare code (Arnouts et al. 1999) with PE-GASE2 stellar synthesis population models library (Fioc & Rocca-Volmerange 1999) for fitting (the redshift was left free to vary)

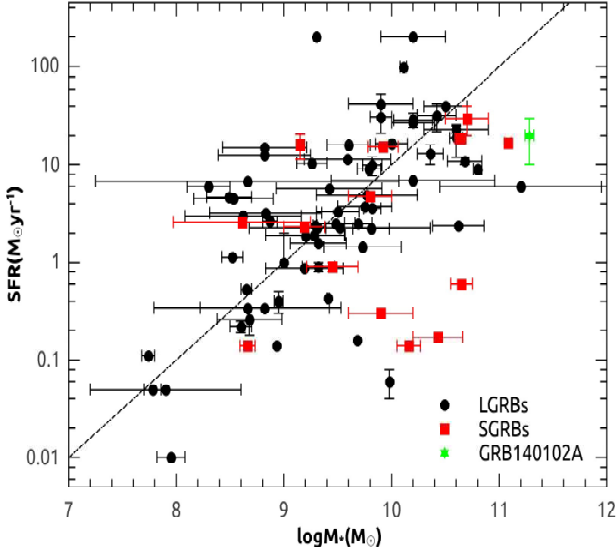


Figure 13. The distribution of SFR a function of stellar mass for a sample of GRB hosts, inferred from template fitting to their photometric SEDs. A green star shows the host position for GRB 140102A. Black dots and red squares indicate the LGRBs, and SGRBs hosts with SFRs measured from GHostS from 1997 to 2014 (Savaglio et al. 2006, 2009). The dashed line shows a constant SSFR of 1 Gyr^{-1} .

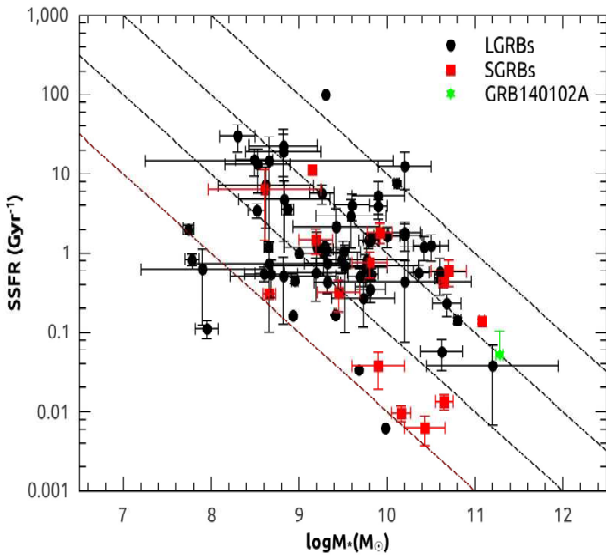


Figure 14. The distribution of SSFR as a function of stellar mass for a sample of GRB hosts, inferred from template fitting to their photometric SEDs. A green star shows the host position for GRB 140102A. Black dots and red squares show GRB hosts with SFRs measured from GHostS from 1997 to 2014 (Savaglio et al. 2006, 2009). The dashed lines show the constant SSFRs of 0.1, 1, 10, and 100 M yr^{-1} from left to right.

the measured photometric magnitudes values of the host galaxy though with large errors associated with photometry. The best solution (see Figure 12) was revealed for redshift $2.8^{+0.7}_{-0.9}$, $E(B-V) = 0.05 \pm 0.05$, and $\chi^2 = 0.1$ with parameters of host galaxy: age of the stellar population in the galaxy $= 9.1 \pm 0.1 \text{ Gyr}$, stellar mass $= (1.9 \pm 0.2) \times 10^{11} \text{ M}_{\odot}$, and SFR (star formation rate) $= 20 \pm 10 \text{ M}_{\odot} \text{ yr}^{-1}$. We find that LePhare host redshift is consistent with the redshift value obtained in § 2.5.1 using joint X-ray and Optical afterglow SED. Furthermore, we compare these properties with other well studied samples of GRB host galaxies. We find that the SFR is higher than the median value of $2.5 \text{ M}_{\odot} \text{ yr}^{-1}$ (Savaglio et al. 2009). The host galaxy of GRB 140102A lies at the upper right position in the stellar mass and SFR correlation plane for star-forming galaxies (see Figure 13; Daddi et al. 2007), indicating the higher mass of the host galaxy than other semi-SFR galaxies. We calculated the specific star formation rate (SSFR) of the host galaxies of GRB 140102A and find that it is lower than the average value of 0.8 G yr^{-1} , but it is consistent (lies towards the lower edge) with the correlation between the stellar mass and the SSFRs (see Figure 14; Savaglio et al. 2009).

4 DISCUSSION

Based on the above results, we extend discussions about important aspects of GRB 140102A and possible implications towards our understanding about early time optical afterglows by comparing with a near-complete sample of LGRBs, listed in Table 5, exhibiting RS emission signatures.

4.1 Afterglow behavior using Closure relationship

Comparison of the temporal slopes derived using power-law fits between the optical and X-ray light curves of GRB 140102A throughout reveals an apparent mismatch. The optical emission has a steep to shallow transition, as predicted in the standard external shock model of RS and FS for a thin shell case. The optical light curve also displays a late time break. The X-ray emission exhibits a normal decay followed by a steeper decay. The optical and X-ray light curves are chromatic in behavior.

To further investigate the chromatic nature of X-ray and optical afterglow, we performed a joint spectral analysis of the available simultaneous multiwavelength data. We created SEDs in five temporal segments, shown in Figure 5. The first two temporal segments are for the RS dominant phase (SED 1 and SED 2), and the last three segments are the FS dominant phase (SED 3, SED 4, and SED 5). We describe the joint spectral analysis method in § 2.5 and present the results in Figure 6. The SED 1 is produced from the data observed with *Swift* BAT and extrapolated the index towards lower (optical) and higher (γ -ray) energies, which covers from $1.98 \times 10^{-3} \text{ keV}$ to $5.5 \times 10^5 \text{ keV}$. We used $\alpha_{\text{opt}} - \beta_{\text{opt}}$, $\alpha_{\text{x-ray}} - \beta_{\text{x-ray}}$ closure relations of RS and FS (Gao et al. 2013) to constrain the p value and position of the cooling-break frequency (ν_c) in the slow cooling case of synchrotron spectrum for an ISM-like medium. We notice that the observed LAT flux is lower than the extrapolated value during SED 1, indicating the presence of possible spectral break (ν_c) between BAT and LAT frequencies. This is in agreement with spectral regime ($\nu > \max\{\nu_m, \nu_c\}$) for the LAT photons discussed in § 4.1.2. The optical and X-ray emission is consistent with $\nu_{\text{opt}} < \nu_{\text{x-ray}} < \nu_c$ spectral regime. Ajello et al. (2018) found that if the cooling break is either in between the XRT or LAT threshold energy or above this then the source can be detected in LAT band which

can be modelled using synchrotron emission. We calculated the p value using observed value of $\alpha_{\text{opt}} - \beta_{\text{opt}}$, $\alpha_{\text{x-ray}} - \beta_{\text{x-ray}}$ and find $p = 2.33 \pm 0.21$, this is consistent with that calculated from afterglow modelling (see § 3.2.3). The SED 2 is produced from the data observed with BOOTES optical telescope, *Swift* BAT, and *Swift* XRT from $T_0 + 63$ to $T_0 + 100$ sec. We consider a simple power-law model along with galactic and host X-ray absorption components for the joint BAT and XRT spectral analysis. We calculated a photon index of $\Gamma = -1.49 \pm 0.05$ (see Table 4). Therefore, the soft and hard X-ray radiation during this temporal window should be originated from the same component. We calculated the p value using observed value of $\alpha_{\text{opt}} - \beta_{\text{opt}}$, $\alpha_{\text{x-ray}} - \beta_{\text{x-ray}}$ during this temporal window, and find $p = 2.10 \pm 0.21$, this is consistent with that calculated from SED 1.

The SED 3 is produced from the data observed with BOOTES optical telescope, *Swift* UVOT, and *Swift* XRT from $T_0 + 700$ to $T_0 + 1000$ sec. In this case, the X-ray and optical could be described with a simple power-law. The observed value of $\alpha_{\text{opt}} - \beta_{\text{opt}}$, $\alpha_{\text{x-ray}} - \beta_{\text{x-ray}}$ indicates that ν_c was still beyond the ν_{opt} and $\nu_{\text{x-ray}}$ spectral regime. We calculated the redshift and host extinction of the burst using this SED due to the availability of multi-band optical observations during this temporal window. Furthermore, we created two more SEDs (SED 4 and SED 5) at late epochs (23-31 ks and 51-65 ks) using optical and X-ray data. In these cases also, the X-ray and optical could be described with a simple power-law, and it appears that the X-ray and the optical are on the same spectral segment ($\nu_{\text{opt}} < \nu_{\text{x-ray}} < \nu_c$), though their light curve decay slopes are different (1.50 ± 0.02 and 1.11 ± 0.15 for X-ray and optical, respectively). However, they are still consistent within 3 sigma.

4.1.1 Early Optical Afterglow and Reverse shock

The optical afterglow of GRB 140102A faded continuously after the first detection ($T_0 + 29$ sec, using BOOTES-4 robotic telescope) and showed a steep to shallow transition, not a simple power-law behavior as is more usually observed in the light curve of optical afterglow. It is likely that the early optical afterglow light curve is produced by the RS emission, and $\sim T_0 + 100$ sec presents the beginning of the dominance of the FS emission. In the case of GRB 140102A, we do not have optical observations before the peak time, but we constrain the decaying index after the peak as -1.72 ± 0.04 ($\sim T_0 + 100$), and this decay index is consistent with the expected value for RS emission due to a thin shell expanding into the ISM-like medium. The closure relation for the RS II class i.e. $\alpha_{\text{dec,opt}}^R = -(27p+7)/35 = -1.74$ considering the $p = 2.00$ (see Table 5), which is consistent with the observed value. Furthermore, we also estimated the expected value of the rising index of RS component using the closure relation i.e. $\alpha_{\text{ris,opt}}^R = (6p-3)/2 = 4.50$ considering the same value of p .

4.1.2 Origin of the high energy LAT photons

For GRB 140102A, the extended LAT emission becomes softer and marginally brighter (consistent with statistical fluctuation) after the end of GBM keV-MeV emission. This indicates that the LAT GeV emission originated later than the GBM keV-MeV emission and from a different spatial region. In this section, we study the possible external origin and radiation mechanism of detected LAT emission.

To investigate the radiation mechanism of high energy GeV LAT photons, we calculated the maximum photon energy emitted by the synchrotron radiation mechanism in an adiabatic external

forward shock during the decelerating phase in the case of ISM external medium. We used the following expression (see equation 2) from Piran & Nakar (2010):

$$h\nu_{\text{max}} = 9 \text{ GeV} \left(\frac{E_{\text{iso},54}}{n_0} \right)^{1/8} \left(\frac{1+z}{2} \right)^{-5/8} \left(\frac{t}{100} \right)^{-3/8} \quad (2)$$

Where $E_{\text{iso},54} = E_{\text{iso}}/10^{54}$ in ergs, t is the arrival time of the event since T_0 in sec, and n_0 is the ISM density. We consider $n_0 = 0.70 \text{ cm}^{-3}$ for the present analysis (see Table 5). We noticed that some of the late time photons (even one photon with source association probability $> 90\%$) lies above the maximum synchrotron energy. It indicates the non-synchrotron origin of these photons. Photons above the maximum synchrotron energy from recent VHE detected GRBs confirms the Synchrotron self-Compton origin for these high energy photons (MAGIC Collaboration et al. 2019; Abdalla et al. 2019; Zhang 2019).

Further, we fitted the LAT energy and photon flux light curves (see Figure 2) obtained from the time-resolved analysis with a simple power-law decay model, which shows that emission could be continuously decreasing with time in both energy and photon fluxes during the temporal bins after the prompt phase ($T_0 + 5$ sec): 5 – 10 sec, 10 – 100 sec, and 100 – 1000 sec. The *Fermi* LAT photon flux light curve shows temporal variation as a power law with an index -1.47 ± 0.01 and the energy flux light curve shows temporal variation as a power law with an index -1.29 ± 0.06 . The LAT photon index (Γ_{lat}) is -2.18 ± 0.08 from a spectral fit obtained by fitting the first 10^5 sec data. This gives spectral index $\beta_{\text{lat}} = \Gamma_{\text{lat}} + 1$ to be -1.18 ± 0.08 . The time-resolved spectra do not show strong temporal variation in the photon index in the first four temporal bins.

In the external shock model, for $\nu > \max\{\nu_m, \nu_c\}$ which is generally true for reasonable shock parameters we can derive the power-law index of the shocked electrons by $f_\nu \propto \nu^{-p/2}$. We have synchrotron energy flux $f_{\text{lat}} \propto \nu^{-\beta_{\text{lat}} - \alpha_{\text{lat}}}$. We found $\alpha_{\text{lat}} = -1.29 \pm 0.06$ (see the LAT light curve in Figure 2) and $\beta_{\text{lat}} = -1.18 \pm 0.08$. The value of β_{lat} gives us $p = 2.36 \pm 0.16$. Thus, the power-law index for the energy flux decay can be predicted by using $f_{\text{lat}} \propto t^{(2-3p)/4}$. The calculated value of α_{lat} is -1.27 ± 0.16 , which agrees well with the observed value of -1.29 ± 0.06 . Hence, we can conclude that for GRB 140102A, the extended LAT high energy afterglow is formed in an external forward shock.

4.2 Derived physical parameters of GRB 140102A and other thin shell cases

In this section, derived parameters of GRB 140102A (T_{dec} and R_B) are compared with other well-studied thin shell cases of optical RS emission. We collected the sample of confirmed optical RS cases consistent with the thin shell in the ISM medium from the literature (see Table 5) to the completeness of the sample. We estimated the expected decay index ($\alpha_{\text{dec,opt}}^R$) using the closure relation i.e. $\alpha_{\text{dec,opt}}^R = -(27p+7)/35$ for RS component, deceleration time (T_{dec}) and radius (R_{dec}) of the blast-wave for each of such events. We used blast-wave kinetic energy, Lorentz factor, circumburst medium density, and redshift parameters from the literature to calculate the T_{dec} and R_{dec} of these bursts. We show the distribution of $\alpha_{\text{dec,opt}}^R$ and R_B with ratio of deceleration time (T_{dec}), and T_{90} duration. Interestingly, we find that GRB 990123 and GRB 061126 do not follow the criteria of the thin shell, i.e., $T_{\text{dec}} > T_{90}$. However, these events have a large value of magnetization parameter ($R_B \gg 1$), and ($\alpha_{\text{dec,opt}}^R$) ~ -2 as excepted from thin shell case of RS component

Table 5. Afterglow modelling results from our theoretical fits for GRB 140102A using the combination of external reverse (RS) and forward shock (FS) model. We also present a sample of confirmed optical RS cases consistent with the thin shell in the ISM ambient medium to compare with the obtained parameters for GRB 140102A. For the present analysis, we have calculated the values of T_{dec} and R_{dec} for all such events. In the case of GRB 161023A, we assume $n = 1 \text{ cm}^{-3}$.

GRB/ (References)	z	T_{90} [sec]	p	Γ_0	$\epsilon_{e,f}$ [10^{-3}]	$\epsilon_{B,f}$ [10^{-5}]	R_B [$\epsilon_{B,r} / \epsilon_{B,f}$]	n_0 [cm^{-3}]	E_K [10^{52} erg]	η_γ	$T_{\text{dec}}/R_{\text{dec}}$ [sec] [$\times 10^{16} \text{ cm}$]
990123 (1, 2, 3)	1.60	63.3	2.49	420	79.0	5	1156	0.3	108.0	$0.2 < \eta_\gamma < 0.9$	36.36/ 14.80
021211 (3, 4, 5)	1.006	2.41	2.20	154	130.0	3	128	9.9	3.0	< 0.6	38.45/ 2.73
060908 (3, 6)	1.884	19.3	2.24	107	14.0	117	72	190.0	2.7	$0.5 < \eta_\gamma < 0.9$	52.64/ 1.25
061126 (3, 7)	1.1588	191	2.02	255	420.0	8	69	3.7	12.0	$0.4 < \eta_\gamma < 0.9$	23.76/ 4.29
080319B (3, 8)	0.937	> 50	2.57	286	68.0	4	16540	0.6	67.6	> 0.6	51.24/ 12.98
081007 (3, 9, 10, 11)	0.5295	8.0	2.72	100	-	-	-	1	79	0.2	592.37/ 23.24
090102 (3, 12, 13)	1.547	27	2.31	228	0.4	2	6666	359.0	816.0	< 0.4	33.57/ 4.11
090424 (3, 10)	0.544	48	2.06	235	2.7	19	25	4.0	258	< 0.6	57.26/ 12.29
130427A (3, 14, 15)	0.34	162.83	2.08	157	3.3	22	4	1.5	521.0	< 0.8	255.34/ 28.18 5
140512A (16, 17, 18)	0.725	154.8	2.25	112.3	290	0.00182	8187	9.7	765	-	490.05/ 21.50
161023A (11, 19)	2.708	80	2.32	140	4	1000	3.2	-	48	-	495.88/ 15.73
180418A (20, 21)	< 1.31	1.5	2.35	160	100	100	14	0.15	0.077	-	30.96/ 3.17
140102A (Present work)	$2.02^{+0.05}_{-0.05}$	$3.58^{+0.01}_{-0.01}$	$2.00^{+0.01}_{-0.01}$	$218.98^{+3.50}_{-3.67}$	$77.0^{+6.7}_{-6.4}$	$420.0^{+50.0}_{-40.0}$	17.75	$0.70^{+0.06}_{-0.05}$	0.12	0.99	18.79/1.78

(1) Bloom et al. (1999); (2) Kippen (1999); (3) Japelj et al. (2014); (4) Vreeswijk et al. (2006); (5) Pizzichini et al. (2005); (6) Palmer et al. (2006); (7) Gomboc et al. (2008); (8) Vreeswijk et al. (2008); (9) Berger et al. (2008); (10) Jin et al. (2013); (11) Yi et al. (2020); (12) de Ugarte Postigo et al. (2009); (13) Gendre et al. (2010); (14) Levan et al. (2013); (15) Barthelmy et al. (2013); (16) de Ugarte Postigo et al. (2014); (17) Sakamoto et al. (2014); (18) Huang et al. (2016); (19) de Ugarte Postigo et al. (2018); (20) Becerra et al. (2019); (21) Fraija et al. (2020).

in the ISM medium. This could be because of the dependency of T_{90} duration on energy range and detector sensitivity. It could also be possible due to the prolonged central engine activity. In the sample of GRBs shown in Figure 15, bursts having RS emission ($T_{\text{dec}} \geq T_{90}$) are considered. It is obvious from the figure that the observed T_{dec} values being spread over more than two magnitudes in time. We also notice that the deceleration radius of these events ranges from $1.25 \times 10^{16} - 2.82 \times 10^{17} \text{ cm}$, suggesting a diverse behavior of ejecta surrounding possible progenitors. A larger sample of GRBs with RS detection is fruitful to understand if a thin shell case leads to dominant RS emission. If the prompt emission is bright, then any sub-dominant early optical afterglow may not be observed. In the case of GRB 140102A, the RS early optical afterglow is found with magnetization parameter $R_B \sim 18$, and this value lies towards lower side of the distribution of magnetization parameter for the sample of RS dominated bursts.

5 SUMMARY AND CONCLUSIONS

We have reported a detailed prompt emission, early afterglow, and host properties of GRB 140102A using the multiwavelength observations. We find a rare and exciting prompt emission spectral evolution where E_p and α_{pt} track the intensity of burst. The observed correlation between E_p and intensity can be understood as the fireball cools and expands. The relativistic fluid loses energy, causing both the electron energy and magnetic field to reduce. The synchrotron energy scale will then naturally reduce, and both intensity and E_p will fall. However, during the bursting phase, the opposite may be possible, and energy supply from the central engine would increase both of these parameters. Recently, Ryde et al. (2019) explain the α_{pt} -intensity correlation in terms of subphotospheric heating in a flow with a varying entropy, all though, in the case of GRB 140102A, we did not find a thermal signature in the

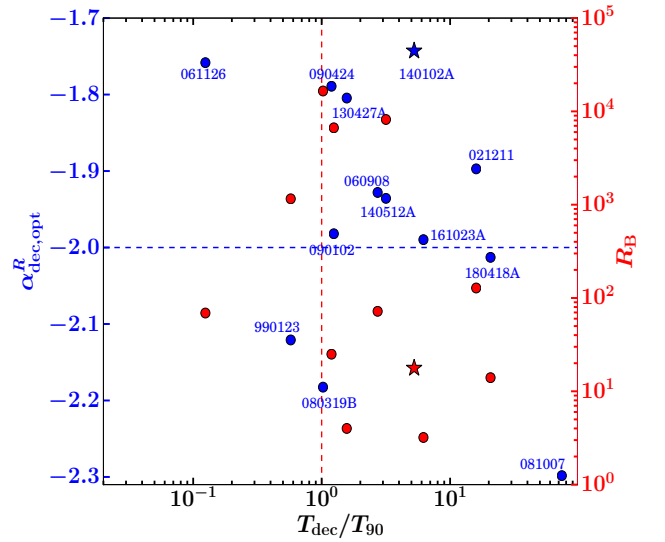


Figure 15. A plot of decaying temporal indices of the RS emission ($\alpha_{\text{dec,opt}}^R$) versus ratio of deceleration time (T_{dec}) and T_{90} duration (left side Y scale) taken from the literature (see Table 5). The right side Y-scale corresponds to the distribution of the magnetization parameter. Blue and red stars show the position of GRB 140102A in this plane. The vertical red dashed line shows a ratio of T_{dec} and T_{90} equal to one. The horizontal blue dashed line represents a line for $\alpha_{\text{dec,opt}}^R = -2.0$.

time-resolved spectroscopy. For this burst, the spectral lag analysis reveals the presence of rarely observed negative lags (Chakrabarti et al. 2018), and it is consistent with the prediction of Uhm et al. (2018), that the negative spectral lag is possible for E_p -intensity

correlation. It will be interesting to examine the spectral evolution-spectral lag correlation for a larger sample of bright bursts with negative spectral lags to understand the emission mechanism of prompt emission better.

Our afterglow modelling results suggest that the early ($\sim 30 - 100$ sec), bright optical emission of GRB 140102A can be well described with the RS model, and the late emission can be explained with the FS model. The RS model parameters for the early optical emission are useful to understand the magnetic energy available in the jet and the source environment (Kobayashi & Zhang 2003; Kobayashi & Sari 2000). We find that the value of $\epsilon_{B,r}$ is larger than $\epsilon_{B,f}$, which provides the value of magnetization parameter $R_B \approx 18$. It demands a moderately magnetized baryonic jet-dominated outflow for GRB 140102A, similar to other cases of RS-dominated bursts (Japelj et al. 2014; Gao et al. 2015). We find a lower value of electron equipartition parameter for the reverse shock ($\epsilon_{E,r}$) than the commonly assumed value of $\epsilon_{E,r} = 0.1$. Gao et al. (2015) suggest that a lower electron equipartition parameter in the external shock would lighten the ‘low-efficiency problem’ of the internal shock model. We calculated the radiative efficiency ($\eta = E_{\gamma,iso}/(E_{\gamma,iso} + E_k)$) value equal to 0.99 for GRB 140102A. Our model predicts a slightly lower X-ray flux during the early phase, similar to other cases of RS-dominated bursts. It might be some intrinsic property of the source, either the central engine activity or wavelength-dependent origin (Yi et al. 2013). It will be beneficial to investigate the possible origin of excess X-ray emission for a larger sample in the near future. The closure relations indicate that the optical and X-ray emission is consistent with $\nu_{opt} < \nu_{x-ray} < \nu_c$ spectral regime for a slow cooling and ISM ambient medium. However, the observed LAT flux during the first SED lies below the extrapolated power-law decay slope, indicating the presence of a possible spectral break between BAT and LAT frequencies. We compare the physical parameters of GRB 140102A with other well-known cases of RS thin shell in the ISM-like medium and find that GRB 990123 and GRB 061126 have $T_{dec} < T_{90}$ even after a larger value of the magnetization parameter ($R_B \gg 1$, i.e., thin shell case) and observed T_{dec} values being spread over more than two magnitudes in time. We also notice that the deceleration radius of these events spread over more than a magnitude (Table 15), suggesting a diverse behavior of ejecta surrounding possible progenitors.

The host galaxy SED modelling suggests that the measured redshift value ($z = 2.8^{+0.7}_{-0.9}$) is consistent with the value obtained from SED. Furthermore, we find that the SFR and stellar mass of the host galaxy of this source is higher than the median value of the sample for star-forming galaxies studied by Savaglio et al. (2009). Overall, GRB 140102A provides a detailed insight into prompt spectral evolution and early optical afterglow along with GeV emission. In future, many more observations of such early optical afterglows and their multiwavelength modelling of RS-dominated GRBs using different RS parameters might help to resolve the open questions like low-efficiency problem, degree of magnetization, ejecta behavior, and environment, etc.

ACKNOWLEDGEMENTS

We thank the anonymous referee for providing constructive comments. RG, SBP, AA, DB, KM, and VB acknowledge BRICS grant DST/IMRCD/BRICS/PilotCall1/ProFCheap/2017(G) for the financial support. AA also acknowledges funds and assistance provided by the Council of Scientific & Industrial Research (CSIR), India. SRO acknowledges the support of the Spanish Ministry, Project

Number AYA2012-39727-C03-01. VAF was supported by RFBR 19-02-00311A grant. RG thanks Dr. V. Chand and Dr. P. S. Pal for helping in high energy data analysis and Bayesian Block algorithm. We are thankful to Dr. P. Veres for sharing data files related to Figure 8 (a). RG and SBP are also thankful to Dr. Judith Racusin, Prof. Gudlaugur Johannesson, and Prof. Nicola Omodei from the LAT team for their valuable comments and suggestions on the manuscript. This research has made use of data obtained from the High Energy Astrophysics Science Archive Research Center (HEASARC) and the Leicester Database and Archive Service (LEDAS), provided by NASA’s Goddard Space Flight Center and the Department of Physics and Astronomy, Leicester University, UK, respectively. This work is based on observations made with the Gran Telescopio Canarias (GTC), installed at the Spanish Observatorio del Roque de los Muchachos of the Instituto de Astrofísica de Canarias, in the island of La Palma. Also based on observations collected at the Centro Astronómico Hispano-Alemán (CAHA) at Calar Alto, operated jointly by Junta de Andalucía and Consejo Superior de Investigaciones Científicas (IAA-CSIC). The *Fermi* LAT Collaboration acknowledges generous ongoing support from a number of agencies and institutes that have supported both the development and the operation of the LAT as well as scientific data analysis. These include the National Aeronautics and Space Administration and the Department of Energy in the United States, the Commissariat à l’Energie Atomique and the Centre National de la Recherche Scientifique / Institut National de Physique Nucléaire et de Physique des Particules in France, the Agenzia Spaziale Italiana and the Istituto Nazionale di Fisica Nucleare in Italy, the Ministry of Education, Culture, Sports, Science and Technology (MEXT), High Energy Accelerator Research Organization (KEK) and Japan Aerospace Exploration Agency (JAXA) in Japan, and the K. A. Wallenberg Foundation, the Swedish Research Council and the Swedish National Space Board in Sweden. Additional support for science analysis during the operations phase is gratefully acknowledged from the Istituto Nazionale di Astrofisica in Italy and the Centre National d’Études Spatiales in France. This work performed in part under DOE Contract DE-AC02-76SF00515. The part of the work was performed as part of the government contract of the SAO RAS approved by the Ministry of Science and Higher Education of the Russian Federation.

DATA AVAILABILITY

The data used in the present work can be made available based on the individual request to the corresponding authors.

REFERENCES

- Abbott B. P., et al., 2017, *The Astrophysical Journal*, 848, L13
- Abdalla H., et al., 2019, *Nature*, 575, 464
- Acuner Z., Ryde F., Pe’er A., Mortlock D., Ahlgren B., 2020, arXiv e-prints, [p. arXiv:2003.06223](https://arxiv.org/abs/2003.06223)
- Ahlgren B., Larsson J., Valan V., Mortlock D., Ryde F., Pe’er A., 2019, *ApJ*, 880, 76
- Ajello M., et al., 2014, *ApJ*, 789, 20
- Ajello M., et al., 2018, *ApJ*, 863, 138
- Ajello M., et al., 2019, *ApJ*, 878, 52
- Akerlof C., et al., 1999, *Nature*, 398, 400
- Akerlof C. W., Zheng W., Pandey S. B., McKay T. A., 2011, *ApJ*, 726, 22
- Alam S., et al., 2015, *ApJS*, 219, 12
- Amati L., 2006, *MNRAS*, 372, 233

- Arnaud K. A., 1996, in Jacoby G. H., Barnes J., eds, *Astronomical Society of the Pacific Conference Series Vol. 101, Astronomical Data Analysis Software and Systems V*. p. 17
- Arnouts S., Cristiani S., Moscardini L., Matarrese S., Lucchin F., Fontana A., Giallongo E., 1999, *MNRAS*, **310**, 540
- Atwood W. B., et al., 2009, *ApJ*, **697**, 1071
- Band D. L., 1997, *ApJ*, **486**, 928
- Band D., et al., 1993, *ApJ*, **413**, 281
- Barthelmy S. D., et al., 2005, *Space Sci. Rev.*, **120**, 143
- Barthelmy S. D., et al., 2013, GRB Coordinates Network, **14470**, 1
- Barthelmy S. D., et al., 2014, GRB Coordinates Network, **15662**, 1
- Becerra R. L., et al., 2019, *ApJ*, **881**, 12
- Belczynski K., Bulik T., Rudak B., 2002, *ApJ*, **571**, 394
- Berger E., 2009, *ApJ*, **690**, 231
- Berger E., Fox D. B., Cucchiara A., Cenko S. B., 2008, GRB Coordinates Network, **8335**, 1
- Bhat P. N., Fishman G. J., Meegan C. A., Wilson R. B., Kouveliotou C., Paciesas W. S., Pendleton G. N., Schaefer B. E., 1994, *ApJ*, **426**, 604
- Bloom J. S., et al., 1999, *ApJ*, **518**, L1
- Breeveld A. A., Landsman W., Holland S. T., Roming P., Kuin N. P. M., Page M. J., 2011, in J. E. McEnery, J. L. Racusin, & N. Gehrels ed., *American Institute of Physics Conference Series Vol. 1358, American Institute of Physics Conference Series*. pp 373–376 ([arXiv:1102.4717](https://arxiv.org/abs/1102.4717)), doi:10.1063/1.3621807
- Bruel P., Burnett T. H., Digel S. W., Johannesson G., Omodei N., Wood M., 2018, *arXiv e-prints*, p. [arXiv:1810.11394](https://arxiv.org/abs/1810.11394)
- Buchner J., et al., 2014, *A&A*, **564**, A125
- Burgess J. M., 2014, *MNRAS*, **445**, 2589
- Burgess J. M., Bégué D., Greiner J., Giannios D., Bacić A., Berlato F., 2020, *Nature Astronomy*, **4**, 174
- Burrows D. N., et al., 2005, *Space Sci. Rev.*, **120**, 165
- Castro-Tirado A. J., et al., 2012, in *Astronomical Society of India Conference Series*. pp 313–320
- Cepa J., et al., 2000, in Iye M., Moorwood A. F., eds, *Society of Photo-Optical Instrumentation Engineers (SPIE) Conference Series Vol. 4008, Optical and IR Telescope Instrumentation and Detectors*. pp 623–631
- Chakrabarti A., Chaudhury K., Sarkar S. K., Bhadra A., 2018, *Journal of High Energy Astrophysics*, **18**, 15
- Chand V., et al., 2018, *ApJ*, **862**, 154
- Chand V., et al., 2020, *ApJ*, **898**, 42
- Chattopadhyay T., Misra R., Chattopadhyay A. K., Naskar M., 2007, *ApJ*, **667**, 1017
- Crider A., et al., 1997, *ApJ*, **479**, L39
- Curran P. A., Starling R. L. C., van der Horst A. J., Wijers R. A. M. J., 2009, *MNRAS*, **395**, 580
- Daddi E., et al., 2007, *ApJ*, **670**, 156
- Dai Z. G., Cheng K. S., 2001, *Astrophys. J. Letters*, **558**, L109
- Davies M. B., Levan A. J., Larsson J., King A. R., Fruchter A. S., 2007, in Axelsson M., Ryde F., eds, *American Institute of Physics Conference Series Vol. 906, Gamma-Ray Bursts: Prospects for GLAST*. pp 69–78 ([arXiv:0704.1899](https://arxiv.org/abs/0704.1899)), doi:10.1063/1.2737408
- De Pasquale M., et al., 2007, *Mon. Not. R. Astr. Soc.*, **377**, 1638
- Duan M.-Y., Wang X.-G., 2020, *ApJ*, **890**, 90
- Evans P. A., et al., 2007, *Astron. Astrophys.*, **469**, 379
- Evans P. A., et al., 2009, *Mon. Not. R. Astr. Soc.*, **397**, 1177
- Fana Dirirsa F., et al., 2019, *ApJ*, **887**, 13
- Fioc M., Rocca-Volmerange B., 1999, *arXiv e-prints*, pp astro-ph/9912179
- Fraija N., Laskar T., Dichiaia S., Beniamini P., Duran R. B., Dainotti M. G., Becerra R. L., 2020, *ApJ*, **905**, 112
- Gao H., Mészáros P., 2015, *Advances in Astronomy*, **2015**, 192383
- Gao H., Lei W.-H., Zou Y.-C., Wu X.-F., Zhang B., 2013, *New Astron. Rev.*, **57**, 141
- Gao H., Wang X.-G., Mészáros P., Zhang B., 2015, *ApJ*, **810**, 160
- Gehrels N., Razzaque S., 2013, *Frontiers of Physics*, **8**, 661
- Gehrels N., et al., 2004, *ApJ*, **611**, 1005
- Gendre B., et al., 2010, *MNRAS*, **405**, 2372
- Goad M. R., Osborne J. P., Beardmore A. P., Evans P. A., 2014, GRB Coordinates Network, **15657**, 1
- Goldstein A., Preece R. D., Mallozzi R. S., Briggs M. S., Fishman G. J., Kouveliotou C., Paciesas W. S., Burgess J. M., 2013, *ApJS*, **208**, 21
- Goldstein A., et al., 2017, *ApJ*, **848**, L14
- Golenetskii S. V., Mazets E. P., Aptekar R. L., Ilinskii V. N., 1983, *Nature*, **306**, 451
- Golenetskii S., Aptekar R., Frederiks D., Pal’Shin V., Oleynik P., Ulanov M., Svinkin D., Cline T., 2014, GRB Coordinates Network, **15667**, 1
- Golkhou V. Z., Butler N. R., Littlejohns O. M., 2015, *ApJ*, **811**, 93
- Gomboc A., et al., 2008, *ApJ*, **687**, 443
- Hagen L. M. Z., et al., 2014, GRB Coordinates Network, **15653**, 1
- Hakkila J., Haglin D. J., Pendleton G. N., Mallozzi R. S., Meegan C. A., Roiger R. J., 2000, *ApJ*, **538**, 165
- Hewett P. C., Warren S. J., Leggett S. K., Hodgkin S. T., 2006, *MNRAS*, **367**, 454
- Horváth I., Tóth B. G., 2016, *Ap&SS*, **361**, 155
- Horváth I., Balázs L. G., Bagoly Z., Veres P., 2008, *A&A*, **489**, L1
- Hu Y. D., et al., 2019, *A&A*, **632**, A100
- Hu Y. D., et al., 2021, *A&A*, **646**, A50
- Huang X.-L., Xin L.-P., Yi S.-X., Zhong S.-Q., Qiu Y.-L., Deng J.-S., Wei J.-Y., Liang E.-W., 2016, *ApJ*, **833**, 100
- Japelj J., et al., 2014, *ApJ*, **785**, 84
- Jin Z.-P., et al., 2013, *ApJ*, **774**, 114
- Joshi J. C., Razzaque S., 2019, *arXiv e-prints*, p. [arXiv:1911.01558](https://arxiv.org/abs/1911.01558)
- Kann D. A., et al., 2010, *ApJ*, **720**, 1513
- Kargatis V. E., Liang E. P., Hurley K. C., Barat C., Eveno E., Niel M., 1994, *ApJ*, **422**, 260
- Kass R. E., Rafferty A. E., 1995, *J. Am. Stat. Assoc.*, **90**, 773
- Kimura M., et al., 2014, GRB Coordinates Network, **15663**, 1
- Kippen R. M., 1999, GRB Coordinates Network, **224**, 1
- Kobayashi S., Sari R., 2000, *ApJ*, **542**, 819
- Kobayashi S., Zhang B., 2003, *ApJ*, **597**, 455
- Kopač D., et al., 2013, *ApJ*, **772**, 73
- Kouveliotou C., Meegan C. A., Fishman G. J., Bhat N. P., Briggs M. S., Koshut T. M., Paciesas W. S., Pendleton G. N., 1993, *Astrophys. J. Letters*, **413**, L101
- Kumar P., Zhang B., 2015, *Phys. Rep.*, **561**, 1
- Kumar A., et al., 2021, *MNRAS*, **502**, 1678
- Laros J. G., et al., 1985, *ApJ*, **290**, 728
- Laskar T., Berger E., Margutti R., Perley D., Zauderer B. A., Sari R., Fong W.-f., 2015, *ApJ*, **814**, 1
- Levan A. J., Cenko S. B., Perley D. A., Tanvir N. R., 2013, GRB Coordinates Network, **14455**, 1
- Levan A., Crowther P., de Grijs R., Langer N., Xu D., Yoon S.-C., 2016, *Space Sci. Rev.*, **202**, 33
- Li Y., Zhang B., Lü H.-J., 2016, *ApJS*, **227**, 7
- Li L., et al., 2019, *ApJ*, **884**, 109
- Lien A., et al., 2016, *ApJ*, **829**, 7
- Lyman J. D., et al., 2017, *MNRAS*, **467**, 1795
- Lytikov M., Blackman E. G., 2001, *MNRAS*, **321**, 177
- MAGIC Collaboration et al., 2019, *Nature*, **575**, 455
- MacFadyen A. I., Woosley S. E., 1999, *ApJ*, **524**, 262
- MacLachlan G. A., et al., 2013, *MNRAS*, **432**, 857
- Meegan C., et al., 2009, *ApJ*, **702**, 791
- Mészáros P., 2019, *Mem. Soc. Astron. Italiana*, **90**, 57
- Mészáros P., Rees M. J., 1997, *Astrophys. J.*, **476**, 232
- Mészáros P., Rees M. J., 1999, *MNRAS*, **306**, L39
- Minaev P. Y., Pozanenko A. S., 2017, *Astronomy Letters*, **43**, 1
- Minaev P. Y., Pozanenko A. S., 2020, *MNRAS*, **492**, 1919
- Minaev P. Y., Pozanenko A. S., Loznikov V. M., 2010, *Astrophysical Bulletin*, **65**, 326
- Minaev P. Y., Pozanenko A. S., Molkov S. V., Grebenev S. A., 2014, *Astronomy Letters*, **40**, 235
- Mukherjee S., Feigelson E. D., Jogesh Babu G., Murtagh F., Fraley C., Raftery A., 1998, *ApJ*, **508**, 314
- Nakar E., Piran T., 2004, *MNRAS*, **353**, 647
- Narayana Bhat P., et al., 2016, *ApJS*, **223**, 28
- Nava L., et al., 2012, *MNRAS*, **421**, 1256

- Norris J. P., Share G. H., Messina D. C., Dennis B. R., Desai U. D., Cline T. L., Matz S. M., Chupp E. L., 1986, *ApJ*, **301**, 213
- Norris J. P., Marani G. F., Bonnell J. T., 2000, *ApJ*, **534**, 248
- Oates S. R., et al., 2009, *Mon. Not. R. Astr. Soc.*, **395**, 490
- Oates S. R., Page M. J., De Pasquale M., Schady P., Breeveld A. A., Holland S. T., Kuin N. P. M., Marshall F. E., 2012, *MNRAS*, **426**, L86
- Obergaulinger M., Aloy M. Á., 2020, *MNRAS*, **492**, 4613
- Oganessian G., Nava L., Ghirlanda G., Melandri A., Celotti A., 2019, *A&A*, **628**, A59
- Palmer D., et al., 2006, GRB Coordinates Network, **5551**, 1
- Panaitelescu A., 2007, *MNRAS*, **379**, 331
- Panaitelescu A., Kumar P., 2002, *Astrophys. J.*, **571**, 779
- Pandey S. B., Yadav R. K. S., Nanjappa N., Yadav S., Krishna Reddey B., Sahu S., Srinivasan R., 2017, arXiv e-prints, [p. arXiv:1711.05422](https://arxiv.org/abs/1711.05422)
- Pe'er A., 2015, *Advances in Astronomy*, **2015**, 907321
- Pei Y. C., 1992, *Astrophys. J.*, **395**, 130
- Pelassa V., Preece R., Piron F., Omodei N., Guiriec S., 2010, arXiv e-prints, [p. arXiv:1002.2617](https://arxiv.org/abs/1002.2617)
- Peng Z. Y., Yin Y., Bi X. W., Bao Y. Y., Ma L., 2011, *Astronomische Nachrichten*, **332**, 92
- Perna R., Belczynski K., 2002, *ApJ*, **570**, 252
- Piran T., 2004, *Reviews of Modern Physics*, **76**, 1143
- Piran T., Nakar E., 2010, *ApJ*, **718**, L63
- Pizzichini G., Ferrero P., Gianotti F., Morelli E., Hete Team 2005, in Turatto M., Benetti S., Zampieri L., Shea W., eds, *Astronomical Society of the Pacific Conference Series Vol. 342, 1604-2004: Supernovae as Cosmological Lighthouses*, p. 326
- Qin Y.-P., Chen Z.-F., 2013, *MNRAS*, **430**, 163
- Racusin J. L., et al., 2009, *Astrophys. J.*, **698**, 43
- Resmi L., Zhang B., 2016, *ApJ*, **825**, 48
- Roming P. W. A., et al., 2005, *Space Sci. Rev.*, **120**, 95
- Roming P. W. A., et al., 2017, *ApJS*, **228**, 13
- Ryde F., Svensson R., 1999, *ApJ*, **512**, 693
- Ryde F., Yu H.-F., Dereli-Bégué H., Lundman C., Pe'er A., Li L., 2019, *MNRAS*, **484**, 1912
- Sakamoto T., et al., 2007, *ApJ*, **669**, 1115
- Sakamoto T., et al., 2014, GRB Coordinates Network, **16258**, 1
- Sari R., Piran T., 1999, *Astrophys. J.*, **520**, 641
- Sari R., Piran T., Narayan R., 1998, *Astrophys. J. Letters*, **497**, L17
- Savaglio S., Glazebrook K., Le Borgne D., 2006, in Holt S. S., Gehrels N., Nousek J. A., eds, *American Institute of Physics Conference Series Vol. 836, Gamma-Ray Bursts in the Swift Era*, pp 540–545 ([arXiv:astro-ph/0601528](https://arxiv.org/abs/astro-ph/0601528)), doi:10.1063/1.2207951
- Savaglio S., Glazebrook K., Le Borgne D., 2009, *ApJ*, **691**, 182
- Scargle J. D., Norris J. P., Jackson B., Chiang J., 2013, arXiv e-prints, [p. arXiv:1304.2818](https://arxiv.org/abs/1304.2818)
- Schady P., et al., 2007, *Mon. Not. R. Astr. Soc.*, **377**, 273
- Schady P., et al., 2010, *MNRAS*, **401**, 2773
- Schlaflly E. F., Finkbeiner D. P., 2011, *ApJ*, **737**, 103
- Shao L., et al., 2017, *ApJ*, **844**, 126
- Skrutskie M. F., et al., 2006, *AJ*, **131**, 1163
- Sonbas E., Vianello G., Longo F., 2014, GRB Coordinates Network, **15659**, 1
- Starling R. L. C., van der Horst A. J., Rol E., Wijers R. A. M. J., Kouveliotou C., Wiersema K., Curran P. A., Weltevredé P., 2008, *ApJ*, **672**, 433
- Uhm Z. L., Zhang B., Racusin J., 2018, *ApJ*, **869**, 100
- Ukwatta T. N., et al., 2010, *ApJ*, **711**, 1073
- Vianello G., et al., 2015, arXiv e-prints, [p. arXiv:1507.08343](https://arxiv.org/abs/1507.08343)
- Vianello G., Gill R., Granot J., Omodei N., Cohen-Tanugi J., Longo F., 2017, preprint, ([arXiv:1706.01481](https://arxiv.org/abs/1706.01481))
- Vianello G., Gill R., Granot J., Omodei N., Cohen-Tanugi J., Longo F., 2018, *ApJ*, **864**, 163
- Vreeswijk P. M., et al., 2006, *A&A*, **447**, 145
- Vreeswijk P. M., Smette A., Malesani D., Fynbo J. P. U., Milvang-Jensen B., Jakobsson P., Jaunsen A. O., Ledoux C., 2008, GRB Coordinates Network, **7444**, 1
- Wang X.-G., et al., 2015, *ApJS*, **219**, 9
- Wang F.-F., Zou Y.-C., Liu Y., Liao B., Moharana R., 2018, *Journal of High Energy Astrophysics*, **18**, 21
- Wei J.-J., Zhang B.-B., Shao L., Wu X.-F., Mészáros P., 2017, *ApJ*, **834**, L13
- Willingale R., Starling R. L. C., Beardmore A. P., Tanvir N. R., O'Brien P. T., 2013, *MNRAS*, **431**, 394
- Woosley S. E., Bloom J. S., 2006, *ARA&A*, **44**, 507
- Xie L., et al., 2020, *ApJ*, **896**, 4
- Yi S.-X., Wu X.-F., Dai Z.-G., 2013, *ApJ*, **776**, 120
- Yi S.-X., Wu X.-F., Zou Y.-C., Dai Z.-G., 2020, *ApJ*, **895**, 94
- Yonetoku D., Murakami T., Nakamura T., Yamazaki R., Inoue A. K., Ioka K., 2004, *ApJ*, **609**, 935
- Zhang B., 2011, *Comptes Rendus Physique*, **12**, 206
- Zhang B., 2019, *Nature*, **575**, 448
- Zhang B., 2020, *Nature Astronomy*, **4**, 210
- Zhang B. B., Bhat N., 2014, GRB Coordinates Network, **15669**, 1
- Zhang B., Kobayashi S., 2005, *ApJ*, **628**, 315
- Zhang B., Mészáros P., 2004, *International Journal of Modern Physics A*, **19**, 2385
- Zhang B., Kobayashi S., Mészáros P., 2003a, *Astrophys. J.*, **595**, 950
- Zhang B., Kobayashi S., Mészáros P., 2003b, *ApJ*, **595**, 950
- Zhang B., Fan Y. Z., Dyks J., Kobayashi S., Mészáros P., Burrows D. N., Nousek J. A., Gehrels N., 2006, *ApJ*, **642**, 354
- Zhang B.-B., et al., 2012, *ApJ*, **748**, 132
- de Ugarte Postigo A., Jakobsson P., Malesani D., Fynbo J. P. U., Simpson E., Barros S., 2009, GRB Coordinates Network, **8766**, 1
- de Ugarte Postigo A., et al., 2014, GRB Coordinates Network, **16310**, 1
- de Ugarte Postigo A., et al., 2018, *A&A*, **620**, A119

AFFILIATIONS

- ¹ Aryabhata Research Institute of Observational Sciences (ARIES), Manora Peak, Nainital-263002, India
- ² Department of Physics, Deen Dayal Upadhyaya Gorakhpur University, Gorakhpur-273009, India
- ³ School of Physics and Astronomy, University of Birmingham, B15 2TT, UK
- ⁴ Instituto de Astrofísica de Andalucía (IAA-CSIC), Glorieta de la Astronomía s/n, E-18008, Granada, Spain.
- ⁵ Departamento de Ingeniería de Sistemas y Automática, Escuela de Ingenierías, Universidad de Málaga, C. Dr. Ortiz Ramos sn, 29071 Málaga, Spain
- ⁶ School of Astronomy and Space Science, Nanjing University, Nanjing 210093, China
- ⁷ Key Laboratory of Modern Astronomy and Astrophysics (Nanjing University), Ministry of Education, China
- ⁸ Universidad de Granada, Facultad de Ciencias Campus Fuentenueva s/n E-18071 Granada, Spain
- ⁹ Special Astrophysical Observatory of Russian Academy of Sciences, Nizhniy Arkhyz, Russia
- ¹⁰ Crimean Astrophysical Observatory, Russian Academy of Sciences, Nauchnyi, 298409 Russia
- ¹¹ School of Studies in Physics and Astrophysics, Pandit Ravishankar Shukla University, Chattisgarh 492 010, India
- ¹² Center for Research and Exploration in Space Science and Technology (CRESST) and NASA Goddard Space Flight Center, Greenbelt, MD 20771, USA
- ¹³ Department of Physics, University of Maryland, Baltimore County, 1000 Hilltop Circle, Baltimore, MD 21250, USA
- ¹⁴ National Astronomical Observatories, Chinese Academy of Sciences, 20A Datun Road, Chaoyang District, Beijing 100101, China.
- ¹⁵ Yunnan National Astronomical Observatory, Chinese Academy of Sciences, Phoenix Hill, 650011 Kunming, Yunnan, China.
- ¹⁶ Inter-University Center for Astronomy and Astrophysics, Pune, Maharashtra 411007, India
- ¹⁷ Department of Physics, Adiyaman University, 02040 Adiyaman, Turkey.
- ¹⁸ Unidad Asociada Grupo Ciencias Planetarias UPV/EHU-IAA/CSIC,

Departamento de Física Aplicada I, E.T.S., Universidad del País Vasco UPV/EHU, Bilbao, Spain.

¹⁹ Ikerbasque, Basque Foundation for Science, Bilbao, Spain.

²⁰ European Space Astronomy Centre (ESA-ESAC), Camino bajo del Castillo, s/n, Villafranca del Castillo, E-28.692 Villanueva de la Cañada (Madrid), Spain

²¹ Universidad Internacional Valenciana, Valencia, Spain

²² Mullard Space Science Laboratory - University College London, Holmbury Rd, Dorking RH5 6NT, UK

²³ Istituto Astrofisica Spaziale e Fisica Cosmica Palermo (INAF), Palermo, Via U. La Malfa 153, I-90146 Palermo, Italy

²⁴ Astronomical Institute of the Czech Academy of Sciences (ASU-CAS), Fričova 298, 251 65 Ondřejov, CZ

²⁵ Fyzikální ústav AV ČR, Na Slovance 2, CZ-182 21 Praha 8, Czech Republic

²⁶ Space Research Institute, Moscow, Russia

²⁷ INAF, Istituto di Astrofisica e Planetologia Spaziali, via Fosso del Cavaliere 100, I-00133 Rome, Italy

²⁸ Nikolaev National University, Nikolska 24, Nikolaev 54030, Ukraine.

²⁹ Nikolaev Astronomical Observatory, Nikolaev, Ukraine.

³⁰ Centre for Astro-Particle Physics (CAPP) and Department of Physics, University of Johannesburg, PO Box 524, Auckland Park 2006, South Africa

³¹ Indian Institute of Technology Bombay, Powai, Mumbai 400076, India

³² Instituto de Educación Secundaria Beniaján, Departamento de Matemáticas, Avda. Montezahar, 17, 30570 Murcia, Spain.

APPENDIX A: TABLES

These tables belong to the analyses presented in § 2.

²⁷ $\text{erg cm}^{-2} \text{sec}^{-1}$ in 8 keV-30 MeV energy channel

Table A1. *Fermi* LAT high energy emission (> 100 MeV) in different temporal bins for a fit with a power-law model for GRB 140102A. All the photon and energy fluxes has been calculated in the 100.0 – 10000.0 MeV energy range.

Sr. no.	Time (sec)	Index	Energy flux (10^{-8} ergs cm^{-2} sec^{-1})	Photon flux ($\times 10^{-5}$ photons cm^{-2} sec^{-1})	Test Statistic (TS)	Log(likelihood)
(0)	0 - 5	-1.95 ± 0.49	13.4 ± 9.85	16.8 ± 9.45	27	23.98
(1)	5 - 10	-2.47 ± 0.61	9.99 ± 6.39	22.4 ± 10.2	33	17.96
(2)	10 - 100	-2.14 ± 0.50	0.75 ± 0.50	1.20 ± 0.60	23	40.87
(3)	100 - 1000	-1.33 ± 0.32	0.13 ± 0.08	0.06 ± 0.05	32	208.10
(4)	2905 - 7460	-2 (fixed)	< 0.02	< 0.03	1	847.28

Table A2. The best fit model (shown with boldface) between different models used for the time-averaged joint spectral analysis of *Fermi* LAT standard, LAT-LLE, *Fermi* GBM (NaI + BGO), and *Swift* BAT data of GRB 140102A. BB correspond to the Black Body model.

Time (sec)/ Detectors	Model	Parameters				-Log(Likelihood)	AIC	BIC	
(BAT+ GBM +LAT)	bkn2pow	$\Gamma_{1,2,3} = 0.69^{+0.06}_{-0.04}, 1.26^{+0.01}_{-0.01}, 2.47^{+0.03}_{-0.03}$		$E_{b1,b2} = 26.92^{+1.18}_{-1.12}, 146.31^{+3.24}_{-3.94}$		2407.72	4844.22	4903.75	
	SBPL	$\alpha_1 = -0.92^{+0.02}_{-0.01}$		$\alpha_2 = -2.85^{+0.06}_{-0.03}$		$E_0 = 163.28^{+5.94}_{-8.15}$	2435.64	4895.86	
	Band	$\alpha_{pt} = -0.85^{+0.02}_{-0.01}$		$\beta_{pt} = -2.72^{+0.03}_{-0.05}$		$E_p = 190.21^{+2.91}_{-5.55}$	2426.26	4877.11	
	bkn2pow+BB	$\Gamma_{1,2,3} = 0.73^{+0.01}_{-0.01}, 1.49^{+0.03}_{-0.03}, 2.60^{+0.02}_{-0.06}$		$E_{b1,b2} = 26.39^{+0.16}_{-0.15}, 254.72^{+15.42}_{-21.30}$		$kT_{BB} = 32.91^{+1.19}_{-1.18}$	2403.39	4839.80	
	SBPL+BB	$\alpha_1 = -0.58^{+0.10}_{-0.09}$		$\alpha_2 = -2.93^{+0.07}_{-0.04}$		$E_0 = 143.99^{+10.33}_{-12.83}$	2402.90	4834.59	
	Band+BB	$\alpha_{pt} = -0.58^{+0.04}_{-0.04}$		$\beta_{pt} = -2.72^{+0.02}_{-0.07}$		$E_p = 186.57^{+4.31}_{-4.16}$	2398.90	4826.58	
	Band + PL	$\alpha_1 = -0.85^{+0.01}_{-0.01}$		$\alpha_2 = -2.72^{+0.13}_{-0.03}$		$E_p = 190.14^{+1.87}_{-4.27}$	$\Gamma_{PL} = -1.59^{+0.75}_{-0.38}$	2425.75	4880.28

Table A3. Time-resolved spectral fitting of GRB 140102A for Band model based on Bayesian Block using *Fermi* GBM and *Swift* BAT data.

Sr. no.	t_1, t_2 (sec)	α_{pt}	β_{pt}	E_p (keV)	(Flux $\times 10^{-06}$) ²⁷	-Log(likelihood)/BIC
1	0.238, 0.412	$-1.10^{+0.07}_{-0.16}$	$-5.00^{+0.47}_{\infty}$	$144.95^{+35.00}_{-9.17}$	$0.87^{+0.06}_{-0.07}$	-205.74/-361.18
2	0.479, 0.633	$-0.67^{+0.05}_{-0.10}$	$-3.04^{+0.53}_{-0.53}$	$186.44^{+22.28}_{-8.00}$	$2.47^{+0.70}_{-0.50}$	-90.20/-130.09
3	0.633, 0.833	$-0.63^{+0.03}_{-0.06}$	$-2.93^{+0.28}_{-0.25}$	$176.08^{+14.40}_{-2.95}$	$6.83^{+1.10}_{-0.80}$	79.54/209.38
4	0.833, 0.929	$-0.53^{+0.08}_{-0.09}$	$-3.42^{+0.65}_{-0.55}$	$119.08^{+7.53}_{-4.40}$	$5.52^{+0.80}_{-0.40}$	-525.58/-1000.87
5	0.929, 1.118	$-0.92^{+0.07}_{-0.06}$	unconstrained	$104.02^{+6.02}_{-6.82}$	$3.22^{+0.60}_{-0.50}$	-141.75/-233.19
6	1.118, 1.435	$-1.13^{+0.12}_{-0.10}$	$-3.01^{+0.79}_{-0.92}$	$81.63^{+7.26}_{-10.17}$	$1.71^{+1.20}_{-0.50}$	182.80/415.90
7	1.435, 1.758	$-1.23^{+0.16}_{-0.14}$	$-2.65^{+0.40}_{-0.38}$	$62.11^{+7.01}_{-7.48}$	$0.82^{+0.50}_{-0.03}$	184.68/419.66
8	1.758, 2.002	$-0.61^{+0.06}_{-0.07}$	$-2.28^{+0.17}_{-0.15}$	$224.54^{+26.74}_{-18.21}$	$13.44^{+4.00}_{-2.70}$	-175.92/-301.55
9	2.002, 2.420	$-0.58^{+0.03}_{-0.05}$	$-2.71^{+0.18}_{-0.16}$	$199.02^{+12.57}_{-5.80}$	$6.73^{+0.90}_{-0.80}$	665.37/1381.05
10	2.420, 2.968	$-0.60^{+0.02}_{-0.04}$	$-2.81^{+0.21}_{-0.21}$	$249.31^{+15.71}_{-5.96}$	$9.66^{+1.20}_{-0.90}$	837.34/1724.99
11	2.968, 3.138	$-0.47^{+0.07}_{-0.09}$	$-3.51^{+0.97}_{-0.74}$	$145.48^{+11.10}_{-9.22}$	$4.54^{+1.90}_{-0.90}$	-133.23/-216.16
12	3.138, 3.329	$-0.67^{+0.04}_{-0.08}$	$-3.05^{+0.45}_{-0.34}$	$169.12^{+16.12}_{-5.22}$	$3.87^{+0.90}_{-0.50}$	36.92/124.15
13	3.329, 3.515	$-0.40^{+0.10}_{-0.08}$	$-2.83^{+0.34}_{-0.37}$	$125.84^{+7.79}_{-10.19}$	$5.12^{+1.70}_{-1.30}$	-68.46/-86.62
14	3.515, 4.265	$-1.00^{+0.07}_{-0.06}$	unconstrained	$109.35^{+6.27}_{-8.29}$	$1.21^{+0.05}_{-0.06}$	826.85/1704.01
15	4.265, 4.999	$-0.93^{+0.36}_{-0.26}$	$-2.19^{+0.17}_{-0.19}$	$56.21^{+9.74}_{-13.10}$	$0.59^{+0.29}_{-0.22}$	763.89/1578.09

Table A4. Time-resolved spectral fitting of GRB 140102A for Black Body + Band and Cutoff-power law model based on Bayesian block using *Fermi* GBM and *Swift* BAT data.

Sr. no.	t_1, t_2 (sec)	kT (keV)	-Log(likelihood)/BIC	E_c (keV)	Γ_{Cutoff}	-Log(likelihood)/BIC
1	0.238, 0.412	$0.98^{+0.04}_{-0.08}$	-205.88/-348.88	$160.86^{+82.05}_{-23.22}$	$-1.10^{+0.08}_{-0.17}$	-205.74/-367.46
2	0.479, 0.633	$0.38^{+0.08}_{-0.15}$	-90.21/-117.54	$156.30^{+27.69}_{-7.32}$	$-0.72^{+0.04}_{-0.08}$	-89.51/-135.00
3	0.633, 0.833	$0.31^{+0.05}_{-0.07}$	79.54/221.96	$145.64^{+16.51}_{-6.69}$	$-0.68^{+0.04}_{-0.05}$	81.23/206.47
4	0.833, 0.929	$1.86^{+0.08}_{-1.23}$	-525.99/-989.11	$86.51^{+13.23}_{-9.95}$	$-0.57^{+0.10}_{-0.11}$	-525.16/-1006.31
5	0.929, 1.118	$0.85^{+1.37}_{-0.42}$	-141.75/-220.61	$96.07^{+12.46}_{-9.95}$	$-0.92^{+0.07}_{-0.11}$	-141.90/-239.78
6	1.118, 1.435	$0.29^{+0.004}_{-0.06}$	182.28/427.43	$95.85^{+20.67}_{-22.05}$	$-1.14^{+0.13}_{-0.10}$	183.06/410.13
7	1.435, 1.758	unconstrained	184.68/432.24	$89.76^{+40.63}_{-27.21}$	$-1.27^{+0.19}_{-0.20}$	185.54/415.10
8	1.758, 2.002	$0.50^{+0.002}_{-0.20}$	18.45/99.78	$53.88^{+9.97}_{-5.21}$	$-0.59^{+0.11}_{-0.16}$	19.51/83.03
9	2.002, 2.420	$0.24^{+1.96}_{-0.31}$	665.37/1393.62	$164.71^{+13.48}_{-7.11}$	$-0.65^{+0.04}_{-0.03}$	675.42/1394.85
10	2.420, 2.968	$0.98^{+0.29}_{-0.31}$	837.34/1737.56	$200.80^{+12.70}_{-7.11}$	$-0.64^{+0.02}_{-0.03}$	839.88/1723.77
11	2.968, 3.138	$0.80^{+0.04}_{-0.62}$	-133.81/-204.75	$100.57^{+11.97}_{-8.79}$	$-0.50^{+0.06}_{-0.08}$	-133.27/-222.52
12	3.138, 3.329	$0.77^{+1.32}_{-0.04}$	36.92/136.73	$136.84^{+22.57}_{-4.50}$	$-0.70^{+0.03}_{-0.08}$	38.39/120.80
13	3.329, 3.515	unconstrained	-68.46/-74.04	$88.64^{+8.53}_{-7.38}$	$-0.47^{+0.07}_{-0.07}$	-66.57/-89.12
14	3.515, 4.265	$0.61^{+0.01}_{-0.33}$	823.85/1710.58	$109.93^{+15.35}_{-17.51}$	$-1.00^{+0.09}_{-0.07}$	826.83/1697.68
15	4.265, 4.999	$0.47^{+0.008}_{-0.09}$	762.21/1587.29	$115.84^{+50.14}_{-35.62}$	$-1.31^{+0.16}_{-0.16}$	765.86/1575.73

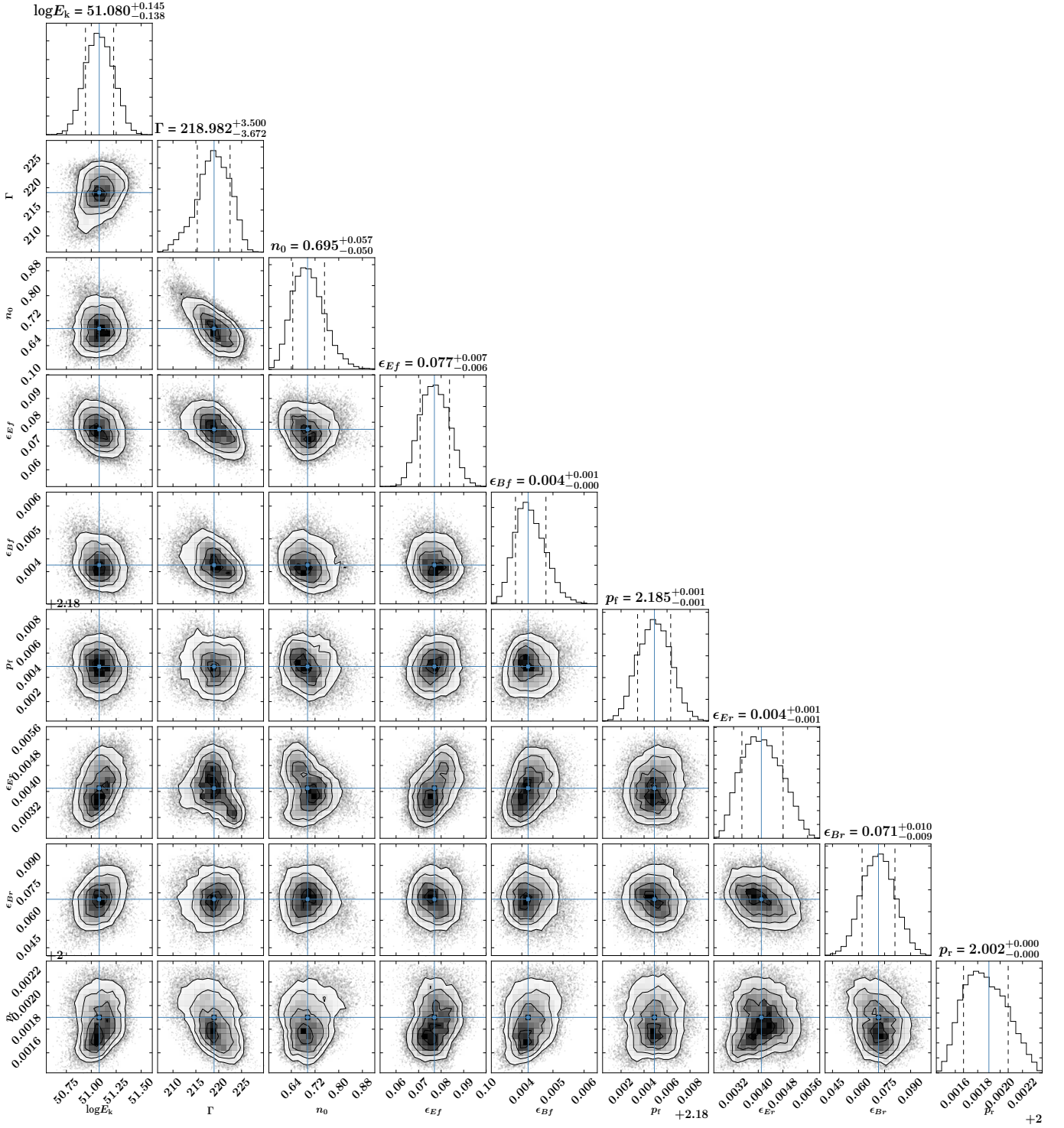


Figure A1. The corner plot has been obtained from the PyMultiNest simulation for each parameter using the thin shell RS and FS afterglow model. The best-fit parameter values in this figure are shown in blue.

Table A5. Log of *Swift* UVOT observations & photometry of GRB 140102A afterglow. No correction for Galactic extinction is applied.

T_{mid} (sec)	Exp. (sec)	Magnitude	Filter	T_{mid} (sec)	Exp. (sec)	Magnitude	Filter
67.82	5.0	$15.67^{+0.07}_{-0.07}$	White	49.90	5.0	$13.97^{+0.11}_{-0.10}$	V
70.32	10.0	$15.70^{+0.05}_{-0.05}$	White	54.47	4.1	$13.98^{+0.12}_{-0.11}$	V
72.82	5.0	$15.74^{+0.07}_{-0.07}$	White	617.37	19.8	$17.21^{+0.36}_{-0.27}$	V
77.82	5.0	$15.83^{+0.07}_{-0.07}$	White	791.14	19.8	$17.61^{+0.52}_{-0.35}$	V
82.82	5.0	$15.99^{+0.08}_{-0.07}$	White	1132.96	192.42	$17.80^{+0.41}_{-0.29}$	V
82.82	15.0	$15.95^{+0.04}_{-0.04}$	White	1479.24	192.11	> 18.58	V
87.82	5.0	$16.02^{+0.08}_{-0.07}$	White	1910.55	364.92	> 18.89	V
92.82	5.0	$16.12^{+0.08}_{-0.07}$	White	2255.54	19.8	> 18.36	V
97.82	5.0	$16.42^{+0.09}_{-0.08}$	White	6733.22	199.8	$19.63^{+0.64}_{-0.40}$	V
100.32	20.0	$16.35^{+0.04}_{-0.04}$	White	11470.66	412.95	$19.66^{+0.40}_{-0.30}$	V
102.82	5.0	$16.29^{+0.08}_{-0.08}$	White	53979.81	199.8	$19.60^{+0.60}_{-0.39}$	V
107.82	5.0	$16.50^{+0.09}_{-0.08}$	White	11470.66	412.9	$19.67^{+0.41}_{-0.30}$	V
112.82	5.0	$16.42^{+0.09}_{-0.08}$	White	53979.81	339.7	> 20.61	V
117.82	5.0	$16.43^{+0.09}_{-0.08}$	White	543.32	19.8	$17.93^{+0.31}_{-0.24}$	B
120.32	20.0	$16.56^{+0.04}_{-0.04}$	White	716.08	19.8	$18.34^{+0.43}_{-0.31}$	B
122.82	5.0	$16.58^{+0.09}_{-0.08}$	White	1231.49	192.2	$18.17^{+0.25}_{-0.21}$	B
127.82	5.0	$16.75^{+0.10}_{-0.09}$	White	1577.50	191.8	$18.38^{+0.35}_{-0.26}$	B
132.82	5.0	$16.74^{+0.10}_{-0.09}$	White	2008.91	364.92	$19.12^{+0.75}_{-0.44}$	B
137.82	5.0	$16.76^{+0.10}_{-0.09}$	White	6117.32	199.8	$19.89^{+0.34}_{-0.26}$	B
142.82	5.0	$16.81^{+0.10}_{-0.09}$	White	7553.81	199.8	$20.26^{+0.73}_{-0.43}$	B
142.82	25.0	$16.83^{+0.04}_{-0.04}$	White	36270.45	907.0	> 21.50	B
147.82	5.0	$16.86^{+0.10}_{-0.09}$	White	61293.68	7811.2	> 22.19	B
152.82	5.0	$16.98^{+0.11}_{-0.10}$	White	288.13	20.0	$17.63^{+0.15}_{-0.13}$	U
157.82	5.0	$16.84^{+0.10}_{-0.09}$	White	308.13	20.0	$17.66^{+0.15}_{-0.13}$	U
162.82	5.0	$16.93^{+0.10}_{-0.09}$	White	328.13	20.0	$17.61^{+0.15}_{-0.13}$	U
167.82	5.0	$17.17^{+0.12}_{-0.11}$	White	348.13	20.0	$17.67^{+0.15}_{-0.13}$	U
170.32	30.0	$17.06^{+0.04}_{-0.04}$	White	368.13	20.0	$17.78^{+0.16}_{-0.14}$	U
172.82	5.0	$17.12^{+0.10}_{-0.10}$	White	388.13	20.0	$18.10^{+0.20}_{-0.17}$	U
177.82	5.0	$17.17^{+0.12}_{-0.10}$	White	408.13	20.0	$18.22^{+0.21}_{-0.18}$	U
182.82	5.0	$17.07^{+0.11}_{-0.10}$	White	428.13	20.0	$17.71^{+0.15}_{-0.13}$	U
187.82	5.0	$17.29^{+0.12}_{-0.11}$	White	448.13	20.0	$18.10^{+0.20}_{-0.17}$	U
192.82	5.0	$17.20^{+0.12}_{-0.11}$	White	468.13	20.0	$18.12^{+0.21}_{-0.17}$	U
197.82	5.0	$17.18^{+0.12}_{-0.11}$	White	488.13	20.0	$18.24^{+0.22}_{-0.18}$	U
200.20	29.76	$17.31^{+0.05}_{-0.05}$	White	508.13	20.0	$18.11^{+0.20}_{-0.17}$	U
202.82	5.0	$17.24^{+0.11}_{-0.11}$	White	523.02	9.8	$18.43^{+0.37}_{-0.28}$	U
207.82	5.0	$17.44^{+0.13}_{-0.12}$	White	308.13	60.0	$17.63^{+0.08}_{-0.08}$	U
212.70	4.8	$17.47^{+0.14}_{-0.12}$	White	368.13	60.0	$17.86^{+0.09}_{-0.09}$	U
567.83	19.75	$18.48^{+0.12}_{-0.11}$	White	438.13	80.0	$18.04^{+0.09}_{-0.08}$	U
740.69	19.75	$18.82^{+0.16}_{-0.14}$	White	503.02	49.8	$18.23^{+0.13}_{-0.12}$	U
931.12	149.76	$19.03^{+0.07}_{-0.06}$	White	691.33	19.8	$18.34^{+0.23}_{-0.19}$	U
1255.78	192.09	$19.23^{+0.15}_{-0.14}$	White	1206.62	192.0	$19.20^{+0.31}_{-0.24}$	U
1602.07	192.42	$19.46^{+0.21}_{-0.18}$	White	1552.79	191.9	$18.90^{+0.27}_{-0.22}$	U
2033.22	364.84	$19.53^{+0.21}_{-0.18}$	White	1984.04	364.7	$19.19^{+0.35}_{-0.27}$	U
6321.93	199.73	$20.68^{+0.23}_{-0.19}$	White	5911.80	199.8	$20.16^{+0.22}_{-0.18}$	U
7758.75	199.77	$21.15^{+0.37}_{-0.37}$	White	7348.47	99.89200	$20.85^{+0.47}_{-0.32}$	U
58406.17	211.27	> 23.89	White	24964.78	725.6	$21.39^{+0.48}_{-0.33}$	U
178945.23	12160.06	> 23.94	White	64529.61	906.8	> 24.15	U
				89761.87	7192.6	> 23.59	U

Table A6: Log of optical photometry observations of GRB 140102A afterglow. The magnitudes have not been corrected for Galactic Extinction $E(B-V)=0.0295$. Magnitudes are in AB based system. Clear filter was calibrated to r filter.

T _{start} (sec)	T _{stop} (sec)	Exposure (sec)	Magnitude	Filter	T _{start} (sec)	T _{stop} (sec)	Exposure (sec)	Magnitude	Filter
29.2	29.7	0.5	12.68 ± 0.23	C	144.3	144.8	0.5	15.24 ± 0.06	C
34.3	34.8	0.5	12.97 ± 0.08	C	146.0	146.5	0.5	15.43 ± 0.07	C
38.9	39.4	0.5	13.20 ± 0.12	C	147.8	148.3	0.5	15.57 ± 0.09	C
40.7	41.2	0.5	13.35 ± 0.27	C	149.5	150.0	0.5	15.59 ± 0.25	C
42.5	43.0	0.5	13.37 ± 0.19	C	151.3	151.8	0.5	15.47 ± 0.15	C
44.2	44.7	0.5	13.45 ± 0.14	C	153.0	153.5	0.5	15.63 ± 0.20	C
45.9	46.4	0.5	13.45 ± 0.34	C	154.8	155.3	0.5	15.66 ± 0.08	C
47.7	48.2	0.5	13.63 ± 0.19	C	156.5	157.0	0.5	15.75 ± 0.15	C
49.4	49.9	0.5	13.54 ± 0.10	C	158.2	158.7	0.5	15.57 ± 0.20	C
51.2	51.7	0.5	13.73 ± 0.14	C	160.0	160.5	0.5	15.59 ± 0.19	C
52.9	53.4	0.5	13.78 ± 0.17	C	161.7	162.2	0.5	15.57 ± 0.25	C
54.7	55.2	0.5	13.87 ± 0.14	C	188.1	193.9	4x0.5	16.04 ± 0.08	C
56.4	56.9	0.5	13.83 ± 0.17	C	195.2	200.9	4x0.5	16.07 ± 0.08	C
58.1	58.6	0.5	13.97 ± 0.09	C	202.2	212.3	4x0.5	16.09 ± 0.12	C
59.9	60.4	0.5	14.03 ± 0.12	C	213.6	219.3	4x0.5	16.15 ± 0.25	C
61.6	62.1	0.5	13.99 ± 0.11	C	220.5	228.1	5x0.5	16.01 ± 0.13	C
63.4	63.9	0.5	14.21 ± 0.15	C	240.6	246.4	4x0.5	16.26 ± 0.08	C
65.1	65.6	0.5	14.16 ± 0.09	C	247.7	253.3	4x0.5	16.36 ± 0.11	C
66.8	67.3	0.5	14.28 ± 0.23	C	255.5	261.3	4x0.5	16.61 ± 0.06	C
68.6	69.1	0.5	14.17 ± 0.05	C	262.6	268.4	4x0.5	16.57 ± 0.06	C
70.4	70.9	0.5	14.26 ± 0.12	C	269.6	277.4	4x0.5	16.69 ± 0.11	C
72.1	72.6	0.5	14.40 ± 0.16	C	278.7	284.4	4x0.5	16.45 ± 0.10	C
73.8	74.3	0.5	14.42 ± 0.09	C	285.6	291.4	4x0.5	16.40 ± 0.09	C
75.6	76.1	0.5	14.49 ± 0.19	C	292.6	298.3	4x0.5	16.75 ± 0.06	C
77.3	77.8	0.5	14.46 ± 0.13	C	299.6	307.1	4x0.5	16.56 ± 0.09	C
79.1	79.6	0.5	14.56 ± 0.12	C	308.3	314.1	4x0.5	16.45 ± 0.10	C
80.8	81.3	0.5	14.51 ± 0.05	C	315.3	321.1	4x0.5	16.72 ± 0.07	C
82.6	83.1	0.5	14.49 ± 0.13	C	322.3	326.3	3x0.5	16.49 ± 0.14	C
84.3	84.8	0.5	14.68 ± 0.15	C	327.8	339.1	2x5.0	16.52 ± 0.08	C
86.1	86.6	0.5	14.73 ± 0.12	C	340.3	351.6	2x5.0	17.03 ± 0.06	C
87.8	88.3	0.5	14.54 ± 0.12	C	352.8	364.1	2x5.0	16.97 ± 0.04	C
89.5	90.0	0.5	14.63 ± 0.11	C	365.3	376.5	2x5.0	16.76 ± 0.04	C
96.9	97.4	0.5	14.84 ± 0.09	C	377.8	389.0	2x5.0	16.89 ± 0.05	C
98.6	99.1	0.5	15.02 ± 0.12	C	390.3	401.5	2x5.0	16.95 ± 0.05	C
100.3	100.8	0.5	14.89 ± 0.12	C	485.3	496.6	2x5.0	17.35 ± 0.10	C
102.1	102.6	0.5	15.10 ± 0.15	C	497.9	509.1	2x5.0	17.34 ± 0.06	C
111.1	111.6	0.5	15.18 ± 0.18	C	510.4	527.2	2x5.0	17.43 ± 0.07	C
112.9	113.4	0.5	15.10 ± 0.12	C	528.4	539.7	2x5.0	17.36 ± 0.09	C
114.7	115.2	0.5	15.23 ± 0.16	C	540.9	552.2	2x5.0	17.39 ± 0.04	C
116.4	116.9	0.5	15.34 ± 0.08	C	553.4	572.2	2x5.0	17.35 ± 0.06	C
118.2	118.7	0.5	15.26 ± 0.16	C	727.6	757.6	30.0	17.75 ± 0.05	C
119.9	120.4	0.5	15.28 ± 0.21	C	758.9	788.9	30.0	17.78 ± 0.03	C
121.6	122.1	0.5	15.28 ± 0.15	C	1082.6	1112.6	30.0	18.17 ± 0.04	C
123.4	123.9	0.5	15.32 ± 0.19	C	1113.9	1143.9	30.0	18.11 ± 0.05	C
125.1	125.6	0.5	15.16 ± 0.17	C	1729.3	1849.3	120.0	18.43 ± 0.06	C
126.9	127.4	0.5	15.28 ± 0.10	C	2037.1	2157.1	120.0	18.62 ± 0.06	C
128.6	129.1	0.5	15.37 ± 0.11	C	2341.6	2461.6	120.0	18.82 ± 0.04	C
130.4	130.9	0.5	15.22 ± 0.24	C	3163.0	3283.0	120.0	18.79 ± 0.05	C
132.1	132.6	0.5	15.58 ± 0.10	C	3470.7	3590.7	120.0	18.96 ± 0.05	C
133.9	134.4	0.5	15.50 ± 0.08	C	3775.2	3895.2	120.0	19.02 ± 0.05	C
135.6	136.1	0.5	15.37 ± 0.27	C	4619.7	4739.7	120.0	18.93 ± 0.04	C
137.3	137.8	0.5	15.54 ± 0.18	C	4978.0	5098.0	120.0	19.14 ± 0.04	C
139.1	139.6	0.5	15.70 ± 0.09	C	5282.5	5402.5	120.0	19.01 ± 0.05	C
140.8	141.3	0.5	15.56 ± 0.20	C	448.7	468.7	20.0	17.66 ± 0.08	g
142.6	143.1	0.5	15.60 ± 0.08	C	622.3	642.3	20.0	17.94 ± 0.04	g
643.6	663.6	20.0	18.04 ± 0.08	g	1853.2	2033.2	180.0	18.56 ± 0.07	r
854.9	914.9	60.0	18.12 ± 0.05	g	3286.8	3466.8	180.0	19.29 ± 0.08	r
1209.9	1269.9	60.0	18.27 ± 0.06	g	4768.9	4948.9	180.0	19.32 ± 0.07	r
2159.4	2339.4	180.0	19.08 ± 0.04	g	918.6	978.6	60.0	18.05 ± 0.13	i
3592.9	3772.9	180.0	19.47 ± 0.05	g	1273.6	1333.6	60.0	18.20 ± 0.11	i
5100.3	5280.3	180.0	19.65 ± 0.05	g	2467.1	2647.1	180.0	18.67 ± 0.07	i
405.3	425.3	20.0	17.35 ± 0.10	r	3900.6	4080.6	180.0	18.60 ± 0.05	i
426.6	446.6	20.0	17.30 ± 0.07	r	5408.0	5588.0	180.0	19.13 ± 0.12	i
578.9	598.9	20.0	17.75 ± 0.16	r	1335.9	1515.9	180.0	17.96 ± 0.15	Z

Table A6: continued.

T_{start} (sec)	T_{stop}(sec)	Exposure (sec)	Magnitude	Filter	T_{start} (sec)	T_{stop}(sec)	Exposure (sec)	Magnitude	Filter
600.2	620.2	20.0	17.71 ± 0.10	r	2649.4	2889.4	240.0	18.81 ± 0.23	Z
792.7	852.7	60.0	18.17 ± 0.08	r	4083.0	4323.0	240.0	19.27 ± 0.21	Z
1147.7	1207.7	60.0	18.57 ± 0.08	r	5590.4	5830.4	240.0	18.98 ± 0.14	Z
5668	5768	100.0	18.99 ± 0.01	R	5794	5894	100.0	19.05 ± 0.05	R
5913	6013	100.0	19.06 ± 0.05	R	96259	98238	300.0×6	22.21 ± 0.27	R

Table A7. Log of the host galaxy observations of GRB 140102A. The tabulated magnitudes are in AB magnitude system and have not been corrected for Galactic extinction.

Date	Exposure (sec)	Magnitude	Filter	Telescope
13.05.2014	59x65.0	21.18 ± 0.26	H	CAHA
18.07.2017	7x120.0	25.13 ± 0.16	g	GTC
18.07.2017	7x90.0	24.47 ± 0.13	r	GTC
18.07.2017	7x90.0	24.17 ± 0.13	i	GTC
18.07.2017	6x60.0	23.88 ± 0.18	z	GTC
16.01.2021	3x300.0, 2x900.0	≥ 24.10	R	3.6m DOT